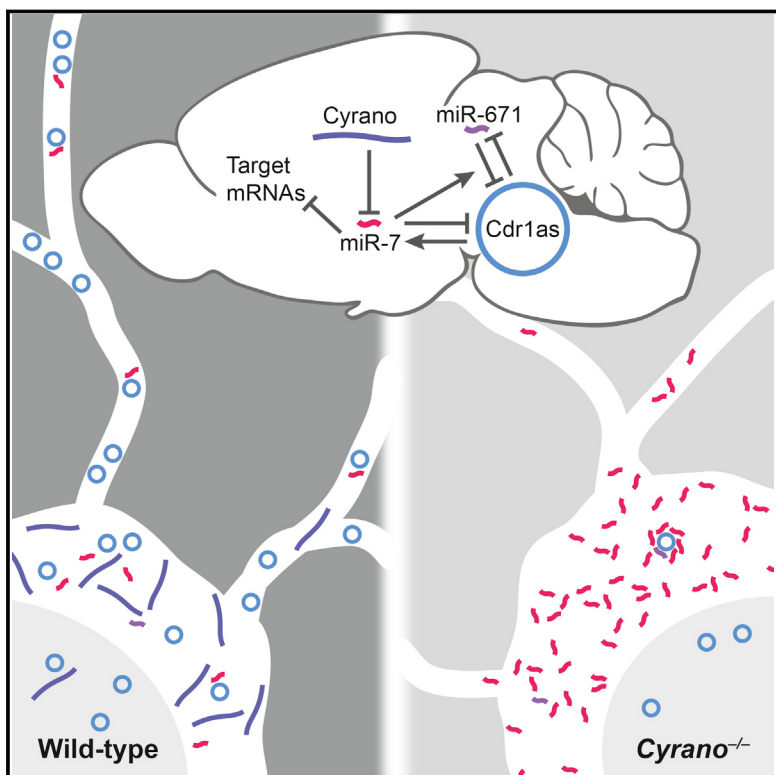


A Network of Noncoding Regulatory RNAs Acts in the Mammalian Brain

Graphical Abstract



Authors

Benjamin Kleaveland, Charlie Y. Shi,
Joanna Stefano, David P. Bartel

Correspondence

dbartel@wi.mit.edu

In Brief

Three different classes of noncoding RNA converge in a regulatory network whereby a long noncoding RNA represses a microRNA via target-directed microRNA degradation, which in turn enables the accumulation of a circular RNA in the mouse brain.

Highlights

- A long noncoding RNA, a circular RNA, and two microRNAs form a regulatory network
- The Cyrano long noncoding RNA directs potent, multiple-turnover destruction of miR-7
- Unchecked miR-7 prevents accumulation of Cdr1as circular RNA in cytoplasm of neurons
- miR-7 prevents this accumulation by enhancing the miR-671-directed slicing of Cdr1as



A Network of Noncoding Regulatory RNAs Acts in the Mammalian Brain

Benjamin Kleaveland,^{1,2,3,4} Charlie Y. Shi,^{1,2,3} Joanna Stefano,^{1,2,3} and David P. Bartel^{1,2,3,5,*}

¹Howard Hughes Medical Institute, Cambridge, MA 02142, USA

²Whitehead Institute of Biomedical Research, Cambridge, MA 02142, USA

³Department of Biology, Massachusetts Institute of Technology, Cambridge, MA 02139, USA

⁴Department of Pathology, Massachusetts General Hospital, Boston, MA, 02114, USA

⁵Lead Contact

*Correspondence: dbartel@wi.mit.edu

<https://doi.org/10.1016/j.cell.2018.05.022>

SUMMARY

Noncoding RNAs (ncRNAs) play increasingly appreciated gene-regulatory roles. Here, we describe a regulatory network centered on four ncRNAs—a long ncRNA, a circular RNA, and two microRNAs—using gene editing in mice to probe the molecular consequences of disrupting key components of this network. The long ncRNA Cyrano uses an extensively paired site to miR-7 to trigger destruction of this microRNA. Cyrano-directed miR-7 degradation is much more effective than previously described examples of target-directed microRNA degradation, which come primarily from studies of artificial and viral RNAs. By reducing miR-7 levels, Cyrano prevents repression of miR-7-targeted mRNAs and enables accumulation of Cdr1as, a circular RNA known to regulate neuronal activity. Without Cyrano, excess miR-7 causes cytoplasmic destruction of Cdr1as in neurons, in part through enhanced slicing of Cdr1as by a second miRNA, miR-671. Thus, several types of ncRNAs can collaborate to establish a sophisticated regulatory network.

INTRODUCTION

MicroRNAs (miRNAs) are abundant ~22 nt (nucleotide) RNAs that regulate gene expression by base-pairing to mRNAs to induce mRNA decay and inhibit translation (Bartel, 2018; Jonas and Izaurralde, 2015). Most miRNAs are extremely stable, with half-lives of days (Bail et al., 2010; Duffy et al., 2015; Gantier et al., 2011; Guo et al., 2015). This stability is attributed to their organization within the effector protein Argonaute, which protects them from exonucleases that degrade naked single-stranded RNAs in the cell. Nonetheless, some miRNAs are destabilized, either constitutively or in response to neuronal excitation or growth factors (Avraham et al., 2010; Hwang et al., 2007; Krol et al., 2010; Rissland et al., 2011).

One way that miRNAs are destabilized is through target RNA-directed miRNA degradation (TDMD). Artificial targets with extensive complementarity to the miRNA can trigger

TDMD through a poorly understood process associated with tailing (addition of untemplated nucleotides) and trimming of the miRNA 3' terminus (Ameres et al., 2010; Baccarini et al., 2011; de la Mata et al., 2015; Denzler et al., 2016; Xie et al., 2012). Natural TDMD triggers are found in some herpesviruses, which use this mechanism to promote degradation of specific host miRNAs (Cazalla et al., 2010; Libri et al., 2012; Marcinowski et al., 2012). In addition, a cellular transcript with TDMD activity limits miR-29b expression in cerebellar granule neurons and regulates behavior in mice and fish (Bitetti et al., 2018).

Long noncoding RNAs (lncRNAs) are transcribed and processed like mRNAs but do not code for functional proteins. Many lncRNAs have been annotated, but few have known functions (Kopp and Mendell, 2018). The lncRNA Cyrano is particularly intriguing because it is broadly conserved in vertebrates and contains a site with unusually high complementarity to the miR-7 miRNA (Ulitsky et al., 2011). Another class of abundant yet enigmatic RNAs is the circular RNAs (circRNAs), which are formed through back-splicing of mRNA or lncRNA exons (Ebbesen et al., 2017). Among the most extensively characterized circRNAs is Cdr1as, which is conserved in mammals and dampens neuronal activity in mice (Hansen et al., 2013; Memczak et al., 2013; Piwecka et al., 2017). Cdr1as has many sites to miR-7 (130 and 73 sites in mouse and human Cdr1as, respectively), the same miRNA that pairs to Cyrano, and Cdr1as and Cyrano are the two RNAs that most frequently cross-link to miR-7 in human and mouse brain (Piwecka et al., 2017). Here, we show that Cyrano promotes unusually efficient destruction of mature miR-7, which enables Cdr1as to accumulate in the brain.

RESULTS

Cyrano Promotes miR-7 Destruction

In zebrafish, Cyrano is expressed throughout the developing nervous system (Ulitsky et al., 2011). In the mouse embryo, Cyrano was also enriched in the early central and peripheral nervous systems (Figure S1A). In adult mice, Cyrano was broadly expressed with 5–10-fold higher expression in brain regions and muscle, a pattern largely conserved in human (Figures S1B and S1C). Within brain, Cyrano appeared more highly expressed in neurons than glia (Figures S1A and S1D), and within cells, Cyrano was mostly in cytoplasm (Figure S1E).



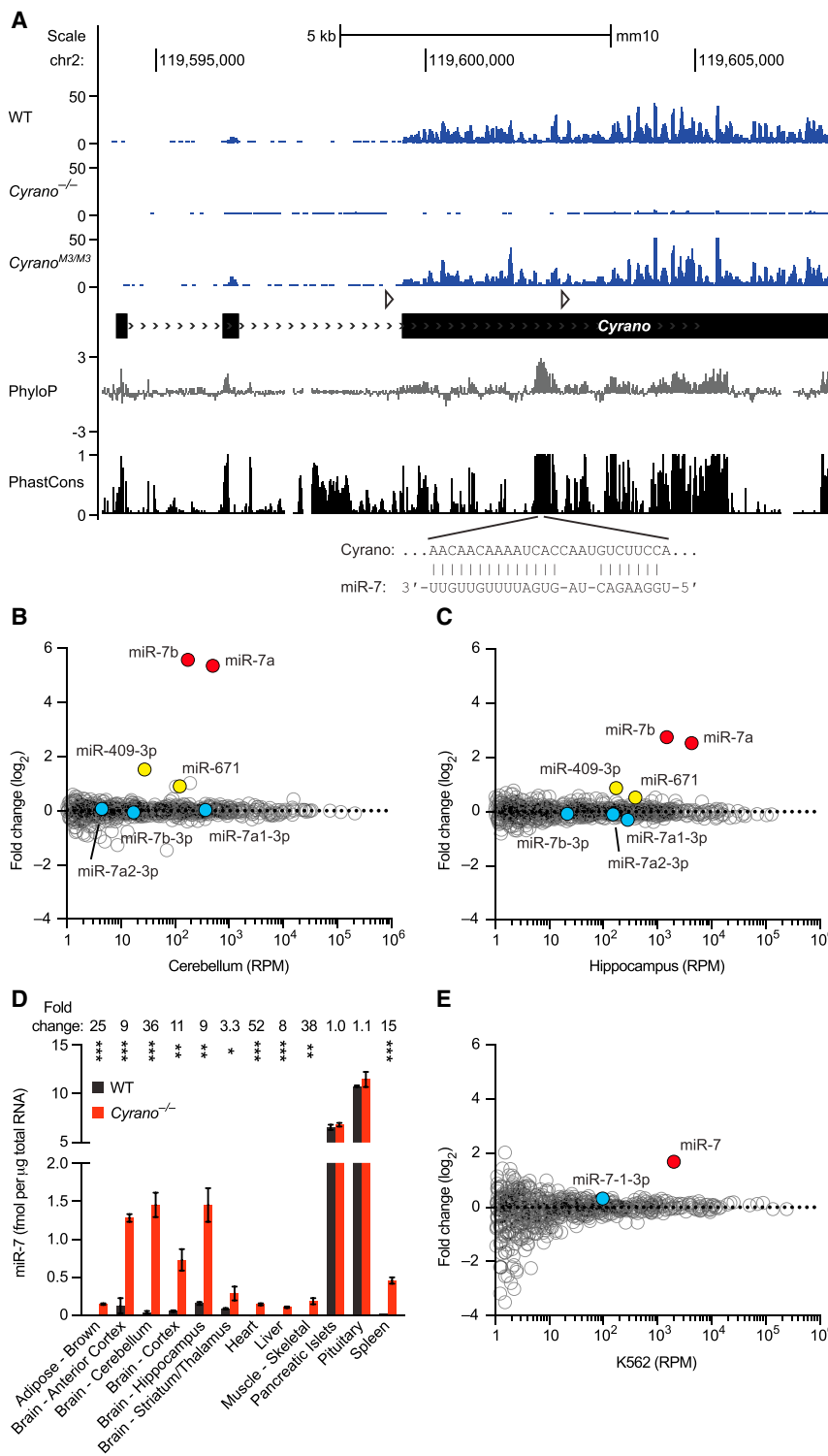


Figure 1. Cyrano Promotes miR-7 Destruction

(A) Organization, conservation, and expression of the murine *Cyrano* locus. Shown below the gene model (black boxes, exons; >>>, introns; open triangles, loxP sites) are conservation plots (PhyloP and PhastCons), which are based on a 40-genome placental mammal alignment generated relative to the mouse locus (Pollard et al., 2010; Siepel et al., 2005). Diagramed below that is the pairing of miR-7 to its highly complementary site, located within the most conserved region of *Cyrano*. Shown above the gene model are RNA-seq tracks for wild-type, *Cyrano*^{-/-}, and *Cyrano*^{M3/M3} cerebellum (y axis, reads) derived from libraries with similar sequencing depths.

(B) Influence of *Cyrano* on miRNA levels in cerebellum. Shown are \log_2 -fold changes in mean miRNA levels observed between wild-type and *Cyrano*^{-/-} cerebellum, as determined by small-RNA sequencing and plotted as a function of expression in wild-type cerebellum ($n = 3$ per genotype). Each circle represents one miRNA, showing results for all miRNAs expressed above 1 RPM (read per million miRNA reads) in wild-type cerebellum. Circles representing miR-7 paralogs, miR-7 passenger strands, and other indicated miRNAs are colored red, blue, and yellow, respectively.

(C) Influence of *Cyrano* on miRNA levels in hippocampus; otherwise, as in (B).

(D) Influence of *Cyrano* on miR-7 levels in 12 mouse tissues. Plotted are mean levels of miR-7 per μ g total RNA for wild-type (black) and *Cyrano*^{-/-} (red) tissues, as determined by northern blots. For each tissue, 3–4 replicates of each genotype were analyzed alongside known quantities of miR-7 synthetic standards (error bars, SD). Statistically significant fold changes are indicated (* $p < 0.05$; ** $p < 0.01$; *** $p < 0.001$, unpaired two-tailed t test).

(E) Influence of *Cyrano* on miRNA levels in K562 cells; otherwise, as in (B).

See also Figures S1 and S2 and Table S1.

To investigate the function of *Cyrano* in mammals, we generated *Cyrano*-deficient mice. The first half of exon 3, which includes the most conserved region of *Cyrano*, was targeted (Figures 1A and S1F). RNA sequencing (RNA-seq) confirmed

complete loss of the targeted region as well as a >90% decrease in flanking *Cyrano* RNA, presumably due to destabilization caused by removal of the final splice site (Figure 1A). *Cyrano*^{-/-} adult mice were born at the expected Mendelian frequency and had no overt abnormalities (Table S1). *Cyrano*^{-/-} adult mice had similar weights and 1-year survival compared to sex-matched littermate controls, and *Cyrano* loss did not seem to affect performance in standard neurobehavioral tests (data not shown). In contrast, *Cyrano* knockdown in zebrafish appears to cause a neurodevelopmental phenotype (Ulitsky et al., 2011), a difference that might be due to the different experimental approaches used to query *Cyrano* loss of function, as reported for other

genes (Kok et al., 2015). Despite their seemingly normal appearance, *Cyrano*^{-/-} mice had striking molecular phenotypes.

The most conserved region of Cyrano contains an unusual site for miR-7 (Figure 1A). In addition to pairing to the miRNA extended seed region (nucleotides 2–8), a common feature of effective miRNA sites (Bartel, 2018), this site has extensive pairing to the remainder of the miRNA (Ulitsky et al., 2011), with only a short internal loop that disrupts pairing to miRNA nucleotides 9 and 10 and should prevent Argonaute2-catalyzed slicing of Cyrano (Elbashir et al., 2001). To determine whether Cyrano deficiency affected accumulation of miR-7 or other miRNAs, we sequenced small RNAs from both wild-type and *Cyrano*^{-/-} brain samples. In humans, all three *MIR7* loci express identical miRNAs, whereas in mice, the three loci express two variants, miR-7a and miR-7b, which differ by a single nucleotide (A or U, respectively) at position 10. In *Cyrano*^{-/-} mice, miR-7a and miR-7b increased 40- and 47-fold in cerebellum and 6- and 7-fold in hippocampus (Figures 1B and 1C). Only two other miRNAs, miR-671 and miR-409-3p, were differentially expressed in both tissues, changing 1.4–2.8-fold.

In principle, increased miR-7 could be caused by (1) increased transcription of *Mir7* genes, (2) enhanced processing of primary or precursor miR-7 RNAs, and/or (3) decreased miR-7 degradation. To distinguish between these possibilities, we examined levels of intermediates in the miRNA-processing pathway. No changes were observed in either primary or precursor miR-7 RNAs in *Cyrano*^{-/-} mice (Figures S2A and S2B). Most importantly, whereas possibilities 1 and 2 would each generate more miRNA duplex (a biogenesis intermediate in which the miRNA is paired to its passenger strand), our small-RNA sequencing results revealed no increase in miR-7 passenger strands (Figures 1B and 1C, species with 3p suffixes), which implied that Cyrano promotes degradation of mature miR-7 after it is loaded into Argonaute.

To further characterize the effect of Cyrano loss on miR-7 levels, we performed northern-blot analyses of samples from 12 adult tissues spanning the range of Cyrano expression (Figure 1D). In *Cyrano*^{-/-} pituitary and pancreatic islets, two tissues with relatively low expression of Cyrano and the highest baseline levels of miR-7, the miR-7 fold changes were not statistically significant. However, in all other Cyrano-deficient tissues tested, miR-7 levels significantly increased, with magnitudes ranging from 3- to 52-fold and increases most prominent in brain tissues. Overall, miR-7 fold changes correlated with Cyrano expression (Figure S2C), as expected if Cyrano exerts greater effects in tissues in which it is more highly expressed. Increased levels of miR-7 were reliably observed in *Cyrano*^{-/-} embryos as early as E13.5 (Figure S2D) and were also observed in primary cultures of *Cyrano*^{-/-} neurons, where they increased 16–45-fold (Figure S2E).

To test whether regulation of miR-7 was conserved in humans, we used CRISPRi (Gilbert et al., 2013) to inhibit CYRANO transcription in human cells. CYRANO reduction in K562 cells led to a specific increase in miR-7, with no significant change in miR-7-3p (Figure 1E). Similar results were also observed in additional human and mouse cell lines, with the increase in miR-7 correlating with the degree of CYRANO knockdown (Figure S2F). These findings confirmed that the ability of Cyrano to destabilize

miR-7 is conserved in humans and requires transcription of the CYRANO locus.

The miR-7 Site in Cyrano Directs Unusually Effective miR-7 Destruction

Based on previous studies of TDMD triggered by artificial and viral transcripts, we suspected that the miR-7 site within Cyrano was crucial for the ability of this endogenous transcript to direct miRNA degradation. To test this, we used Cas9 to generate six mouse lines (M1–M6) with perturbations in the site (Figure 2A). Although some of the mutations were expected to disrupt miR-7 binding (Bartel, 2018), none affected expression of Cyrano in the tissues tested (cerebellum and pituitary) (Figure S3). In contrast, all six disrupted the ability of Cyrano to induce miR-7 degradation (Figure 2B). The M2 and M3 mutations only perturbed miR-7 seed pairing, and mice harboring these mutations had miR-7 increases resembling those of Cyrano-deficient mice, indicating that, as expected, seed pairing is critical for this interaction. More surprisingly, the M1 allele, which had the smallest perturbation, a 2 nt deletion eliminating only a single Watson–Crick pair to the extended seed region and reducing the size of the internal loop from 4 to 3 nucleotides, was also largely unable to promote miR-7 destruction. Overall, the effects of perturbing the miR-7 site demonstrated that Cyrano acts through a form of TDMD reminiscent of that initially observed for artificial and viral transcripts.

One important difference between TDMD mediated by Cyrano and that described previously was its efficacy, as indicated by the decrease in miR-7 molecules per Cyrano molecule observed at steady state. In wild-type cerebellar granule neuron (CGN) cultures, Cyrano was present at 102 ± 16 molecules per cell, and miR-7 was present at 40 ± 7 molecules per cell, whereas in Cyrano-deficient CGNs, miR-7 levels increased 45-fold to 1,800 molecules per cell (Figure S2E; Table S2). These values implied that Cyrano promoted TDMD with multiple turnover, with each Cyrano molecule responsible for destruction of an average of 17 miR-7 molecules ($(1,800 - 40) \div 102$), especially when considering that the insensitivity of Cyrano to perturbation of either miR-7 pairing (Figure S3) or miR-7 abundance (described later) disfavored a model in which Cyrano degradation was coupled to miR-7 degradation. In contrast, similar calculations using values reported for previous examples of TDMD estimated the efficacy of viral HSUR1 to be ~0.1 miR-27 molecules per target (Cazalla et al., 2010; Lee et al., 1988) and that of artificial single-site transcripts to be either 0.1–0.8 miR-122 molecules per target (Denzler et al., 2016) or 0.3–1.0 miRNA molecules per target, with multiple turnover achieved only when artificially boosting the miRNA level (de la Mata et al., 2015). These estimates indicated that Cyrano-promoted TDMD is 17–170 times more effective than that of previously described examples.

To investigate further the specificity of this phenomenon, we examined whether the miR-7-destabilizing activity of Cyrano could be applied to other miRNAs. The 3' UTR of a reporter gene was modified to include a 197 nt fragment of Cyrano, using versions of this region that contained either a wild-type miR-7 site, a mutant miR-7 site, or a site extensively complementary to either miR-16 or miR-17 (Figure 2C). Decreased miR-7 was observed only in cells expressing the wild-type Cyrano region,

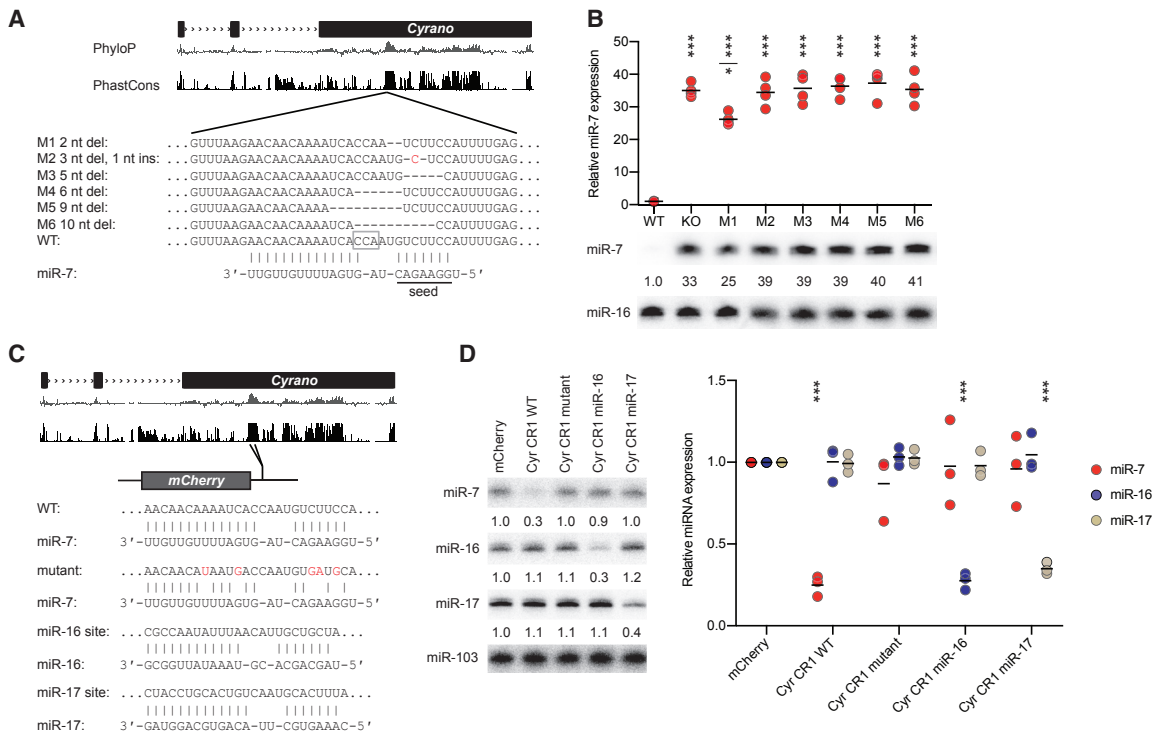


Figure 2. The miR-7 Site in Cyrano Specifies miR-7 Degradation

(A) Schematic of wild-type and Cyrano mutant alleles that alter the extensively paired miR-7 site. Shown below the gene model and conservation tracks are the wild-type Cyrano miR-7 site and six mutant sites, M1–M6. The PAM motif used for mutagenesis is outlined (open gray box). Deleted nucleotides are indicated by dashes; an inserted nucleotide is colored red. The miR-7 extended seed is underlined.

(B) Importance of the miR-7 site for Cyrano function in cerebellum. Bottom: Representative northern blot measuring miR-7 levels in cerebellum of the lines described in (A). In each lane, the level of miR-7 was normalized to that of miR-16 and reported relative to wild-type. Top: Relative miR-7 levels determined from all replicates (black bars, mean; n = 4 per genotype). Statistically significant changes compared to wild-type are indicated (**p < 0.001, ANOVA with Tukey's test). The miR-7 level in M1 cerebellum also differed from that in *Cyrano*^{-/-} (KO) and M2–M6 cerebellum (*p < 0.05, ANOVA with Tukey's test).

(C) Schematic of the wild-type CR1 (Cyrano conserved region) construct and constructs that changed its miR-7 site. The miR-7 site in the CR1 was mutated to either disrupt pairing to miR-7 or introduce an extensively complementary site to miR-16 or miR-17.

(D) Importance of the complementary site for specifying CR1 function. Left: Representative northern blot measuring miR-7, miR-16, and miR-17 levels in HEK293T cells transfected with the constructs described in (C). Below each panel, levels of miRNA are reported relative to levels in the control mCherry transfection after normalizing to the level of miR-103. Right: Relative levels of miR-7 (red), miR-16 (blue), and miR-17 (tan) (black bars, mean; n = 3). Statistically significant changes compared to the mCherry control are indicated (**p < 0.001, ANOVA with Dunnett's test).

See also Figure S3 and Table S2.

whereas decreased miR-16 or miR-17 was observed specifically in cells expressing the region with cognate sites (Figure 2D). These results resembled those of analogous experiments that start with viral or artificial TDMD-triggering transcripts, and like those previous experiments, the amount of degradation was modest, with only ~3-fold reductions of the cognate miRNA observed for our constructs in HEK293T cells—much less than the 45-fold reduction observed for endogenous Cyrano in CGN culture (Figure S2E).

Cyrano Induces Tailing and Trimming of miR-7, but Tailing Appears Dispensable

Tailing and trimming of the miRNA 3' end are often associated with TDMD (Ameres et al., 2010; Baccarini et al., 2011; de la Mata et al., 2015; Denzler et al., 2016; Marcinowski et al., 2012; Xie et al., 2012). Likewise, we found that the fractions of tailed (≥ 25 nt) and trimmed (≤ 22 nt) miR-7 molecules were

greater in wild-type than in *Cyrano*^{-/-} hippocampus and cerebellum (Figures 3A and S4A). Such differences were not observed for any other miRNA with read coverage sufficient for analysis (Figures S4B and S4C), as exemplified by results for miR-92b (Figures 3A and S4A).

In flies, tailing is primarily through addition of untemplated uridines (Ameres et al., 2010, 2011), whereas in mammals, adenylation appears more frequently than uridylylation, although both have been reported (Ameres et al., 2010; Baccarini et al., 2011; de la Mata et al., 2015; Marcinowski et al., 2012; Xie et al., 2012). We found that Cyrano mostly increased the fraction of mature miR-7 reads with two or more untemplated adenosines, whereas monoadenylation and tailing with other nucleotides were less affected (Figures 3A and S4A). These results suggested that the cytoplasmic poly(A) polymerase Gld2 might be responsible for this activity. Indeed, re-analyses of small-RNA sequencing data from wild-type and *Gld2*^{-/-} hippocampus

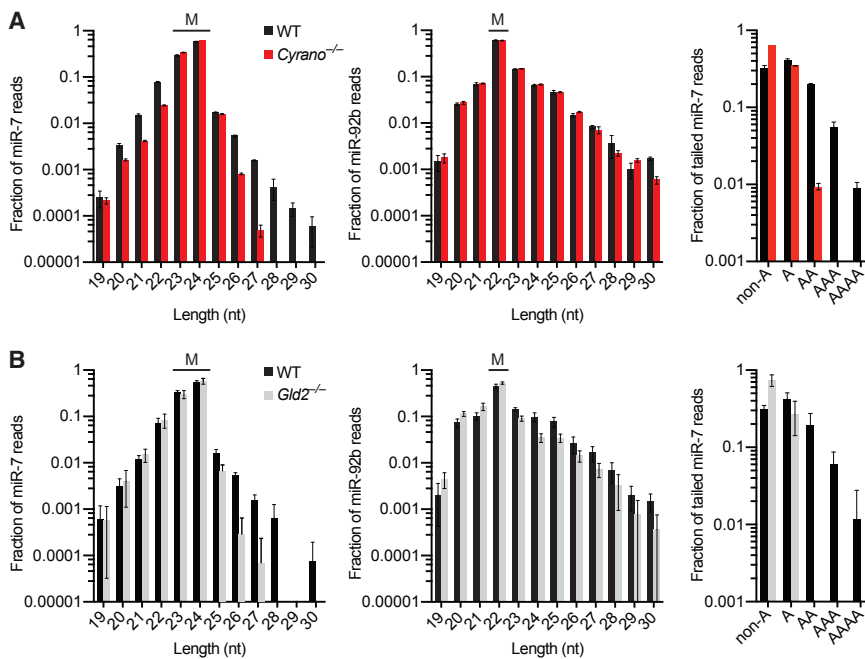


Figure 3. Cyrano Induces Tailing and Trimming of miR-7, but Tailing Appears Dispensable

(A) Influence of Cyrano on miR-7 tailing and trimming in hippocampus. Plotted are length distributions of miR-7 reads (left) and miR-92b reads (middle) from wild-type (black) and *Cyrano*^{-/-} (red) tissue, indicating the mature species for each miRNA (M) (error bars, SD; n = 3 per genotype). Also plotted are the fractions of tailed miR-7 reads that were mono- or oligoadenylylated (right) in wild-type and *Cyrano*^{-/-} tissue.

(B) Influence of *Gld2* on miR-7 tailing and trimming in hippocampus. Primary data from Mansur et al. (2016) were analyzed as in (A), with results for *Gld2*^{-/-} tissue plotted in gray (n = 6 per genotype). See also Figure S4.

For context, we first processed RNA-seq data comparing wild-type to *Mir7a2*^{-/-} pituitary (Ahmed et al., 2017). miR-7 is the most abundant miRNA in pituitary, and deletion of *Mir7a2* leads to greatly reduced miR-7 levels in pituitary, an increase in predicted miR-7 targets,

(Mansur et al., 2016) revealed that *Gld2* deletion substantially reduced the proportion of tailed miR-7 reads and eliminated oligoadenylylated miR-7 reads (Figure 3B). These results for *Gld2* deletion mirrored those observed for *Cyrano* deletion, except the influence of *Gld2* was not specific to miR-7 (Figures 3B and S4D). Although *Gld2* appeared responsible for *Cyrano*-dependent oligoadenylylation of miR-7, unlike loss of *Cyrano* (Figures 3A and S4C), loss of *Gld2* caused no decrease in the proportion of trimmed miR-7 reads (Figures 3B and S4E). Moreover, loss of *Gld2* did not significantly affect levels of any miRNA, including miR-7 (Mansur et al., 2016) (Figure S4F). Likewise CRISPRi stable knockdown of *PAPD4* (the human *Gld2* homolog) by as much as 98% in K562 cells did not affect miR-7 levels (Figure S4G). These results showed that oligoadenylylation observed in the presence of *Cyrano* can be uncoupled from both trimming and degradation of miR-7. Results of additional experiments supported the idea that the miR-7 tailing observed in the presence of *Cyrano* is not on-pathway for *Cyrano*-directed miR-7 degradation (Figures S4H and S4I), which further implied that tailing might not be an obligate step of TDMD.

Loss of *Cyrano* Causes Increased miR-7 Target Repression

The change in miR-7 from very low to intermediate levels in many *Cyrano*-deficient tissues (Figure 1D) raised the question of whether miR-7 targets might be affected. To answer this question, we performed RNA-seq on wild-type and *Cyrano*^{-/-} tissues and compared fold changes of predicted miR-7 targets to fold changes of mRNAs lacking a miR-7 site. The effects on all predicted targets were compared to the effects on both conserved predictions and the top ~80 predictions (Agarwal et al., 2015), expecting greater signal for subsets predicted with higher confidence (i.e., top targets > conserved targets > all targets).

and infertility (Ahmed et al., 2017). Accordingly, we observed significant derepression of predicted miR-7 targets in *Mir7a2*^{-/-} pituitary, with greater derepression for higher-confidence predictions (Figure 4A). When analyzing *Cyrano*^{-/-} tissues, strong evidence for increased miR-7 target repression was observed in three of ten tissues tested—striatum/thalamus, skeletal muscle, and pituitary (Figures 4B and 4C). Detection of increased repression in pituitary suggested that miR-7 increased in pituitary, even though the increase did not pass our threshold for statistical significance when measured by northern blots (Figure 1D). *Cyrano*^{-/-} spleen had an unanticipated increase in predicted miR-7 targets, although this effect did not persist when considering only top predictions. In tissues with increased miR-7 target repression, the amount of repression was substantially less than the effect of deleting miR-7 in pituitary (Figure 4), consistent with our results showing that absolute levels of miR-7 in *Cyrano*-deficient tissues were still ≥ 7 -fold lower than that of wild-type pituitary (Figure 1D). Despite modest effect sizes, these results showed that by limiting miR-7 accumulation, *Cyrano* attenuates repression of miR-7 targets in some tissues.

Cyrano Enables the *Cdr1as* circRNA to Accumulate in the Brain

The statistically significant signal for increased miR-7 repression observed in some *Cyrano*-deficient tissues was attributable to many miR-7 targets being repressed—but each by only a small amount. Indeed, when searching for any genes that on their own were differentially expressed in *Cyrano*^{-/-} cerebellum with adjusted p value < 0.01, only three were identified (Figure 5A). One was *Cyrano*, as expected (Figure 1A), and another was the downstream gene *Nusap1*, which increased due to read-through transcription and aberrant splicing (Figure S5A). The third was the gene for *Cdr1as*, the circRNA with 130 sites

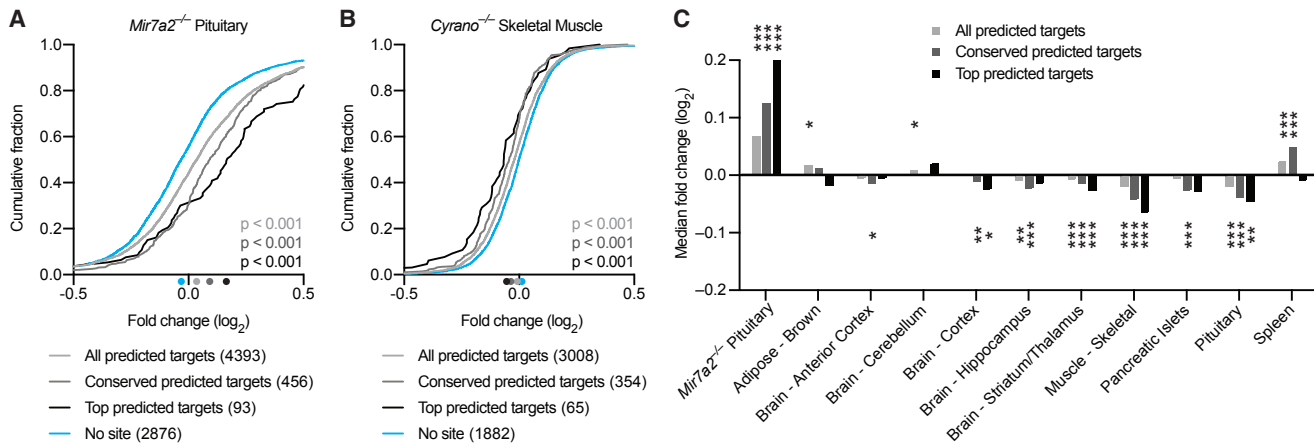


Figure 4. Loss of Cyrano Can Cause Increased miR-7 Target Repression

(A) Repression of predicted miR-7 targets by miR-7a-2 in pituitary. Plotted are cumulative distributions of mRNA fold changes observed after deleting *Mir7a2* in pituitary (Ahmed et al., 2017), comparing the impact on all predicted miR-7 targets (light gray), conserved predicted miR-7 targets (dark gray), and top predicted miR-7 targets (black) to that of control mRNAs with no miR-7 site (blue). Median log₂-fold changes for each set of mRNAs are indicated (colored dots below the x axis). Statistical significance of differences between each set of predicted targets and control mRNAs was determined by the Mann-Whitney test.

(B) Influence of Cyrano on predicted targets of miR-7 in skeletal muscle. Plotted are cumulative distributions of mRNA fold changes observed in skeletal muscle after disrupting *Cyrano*; otherwise, as in (A).

(C) Influence of Cyrano on predicted targets of miR-7 in ten tissues. Plotted are median fold changes observed upon *Cyrano* disruption for the indicated sets of predicted miR-7 targets, normalized to the median fold change of control genes. For reference, effects of deleting *Mir7a2* in pituitary, as evaluated in (A), are also shown (leftmost set of bars). For Cyrano-deficient tissues, the number of genes analyzed in each set ranged from 3,008 to 4,035 (all), 354 to 453 (conserved), 63 to 83 (top), and 1,882 to 2,531 (no site). Statistically significant changes compared to control sets are indicated (*p < 0.05; **p < 0.01; ***p < 0.001, Mann-Whitney test).

to miR-7. Its expression decreased 10-fold in *Cyrano^{-/-}* cerebellum.

Although our RNA-seq libraries were generated after poly(A) selection, which should not efficiently capture circRNAs, very few reads mapped beyond the portion of Cdr1as known to circularize (Figure S5B), suggesting that the RNA-seq was in fact capturing the circular isoform. Moreover, qRT-PCR analysis using primers that spanned the back-splice junction (and were thus specific to the circular isoform) found a similar 10-fold reduction in Cdr1as in Cyrano-deficient cerebellum (Figure 5B). In wild-type mice, Cdr1as is expressed in neurons throughout the brain, with highest expression in cerebellum (Hansen et al., 2013; Memczak et al., 2013; Piwecka et al., 2017) (Figure S5C). Cdr1as levels decreased throughout Cyrano-deficient brain, with the greatest effect observed in cerebellum, followed by cortex, hippocampus, and hypothalamus (Figure 5B), resembling the rank order of miR-7 fold changes in these regions (Figure 1D).

To determine the subcellular location of Cyrano activity, we performed single-molecule FISH (fluorescence *in situ* hybridization), probing for Cyrano and Cdr1as in cultured CGNs, the most abundant neuron in the cerebellum. An average of 100 molecules of Cyrano and 137 molecules of Cdr1as were observed in wild-type CGNs (Figure 5C), which agreed with our qRT-PCR estimates (Table S2). Cyrano was observed predominantly in cytoplasm (73%) with molecules distributed in both soma and processes (Figures S5D and S5E). As previously described in cortical neurons (Piwecka et al., 2017), Cdr1as was also predominantly localized to cytoplasm (86%), with most molecules found in processes (Figure 5D). In *Cyrano^{-/-}* CGNs, a few Cyrano transcripts were detected (Figures S5D and S5E), consistent with our

RNA-seq results (Figure 1C). The number of Cdr1as molecules also decreased in nearly all neurons (Figure 5C), and strikingly, this decrease was entirely attributable to depletion from soma and processes (Figure 5E). The preservation of Cdr1as levels in the nucleus suggested that the large reduction of Cdr1as in *Cyrano^{-/-}* cells occurred through cytoplasmic destruction rather than reduced production or defective export. These results suggested a model in which high levels of miR-7 induce cytoplasmic destruction of Cdr1as, and Cyrano, by limiting miR-7, enables Cdr1as to accumulate in neuronal cell bodies and processes.

Cdr1as Is Regulated by miR-7 and miR-671

To explore further the idea that miR-7 links the fate of Cyrano to that of Cdr1as, we analyzed RNA-seq results from cerebellum of *Cyrano^{M3/M3}* mice, which had a 5 nt deletion in the miR-7 site (Figure 2A). When compared to results from wild-type cerebellum, expression of Cyrano did not change (Figures 6A and 1C), as expected from our previous qRT-PCR analyses (Figure S3). Expression of the downstream gene *Nusap1* also did not change, as expected in this mutant predicted to retain normal Cyrano splicing and 3' end processing. Remarkably, Cdr1as was the only differentially expressed gene identified with adjusted p value < 0.01, and its expression decreased 11-fold in *Cyrano^{M3/M3}* cerebellum, similar to the decrease observed in *Cyrano^{-/-}* cerebellum. This decrease in Cdr1as was corroborated by qRT-PCR analyses of cerebellar samples from all six lines with mutations in the miR-7 site of Cyrano (Figure S6A). These results showed that the miR-7 complementary site within Cyrano is required for this lncRNA to influence Cdr1as accumulation.

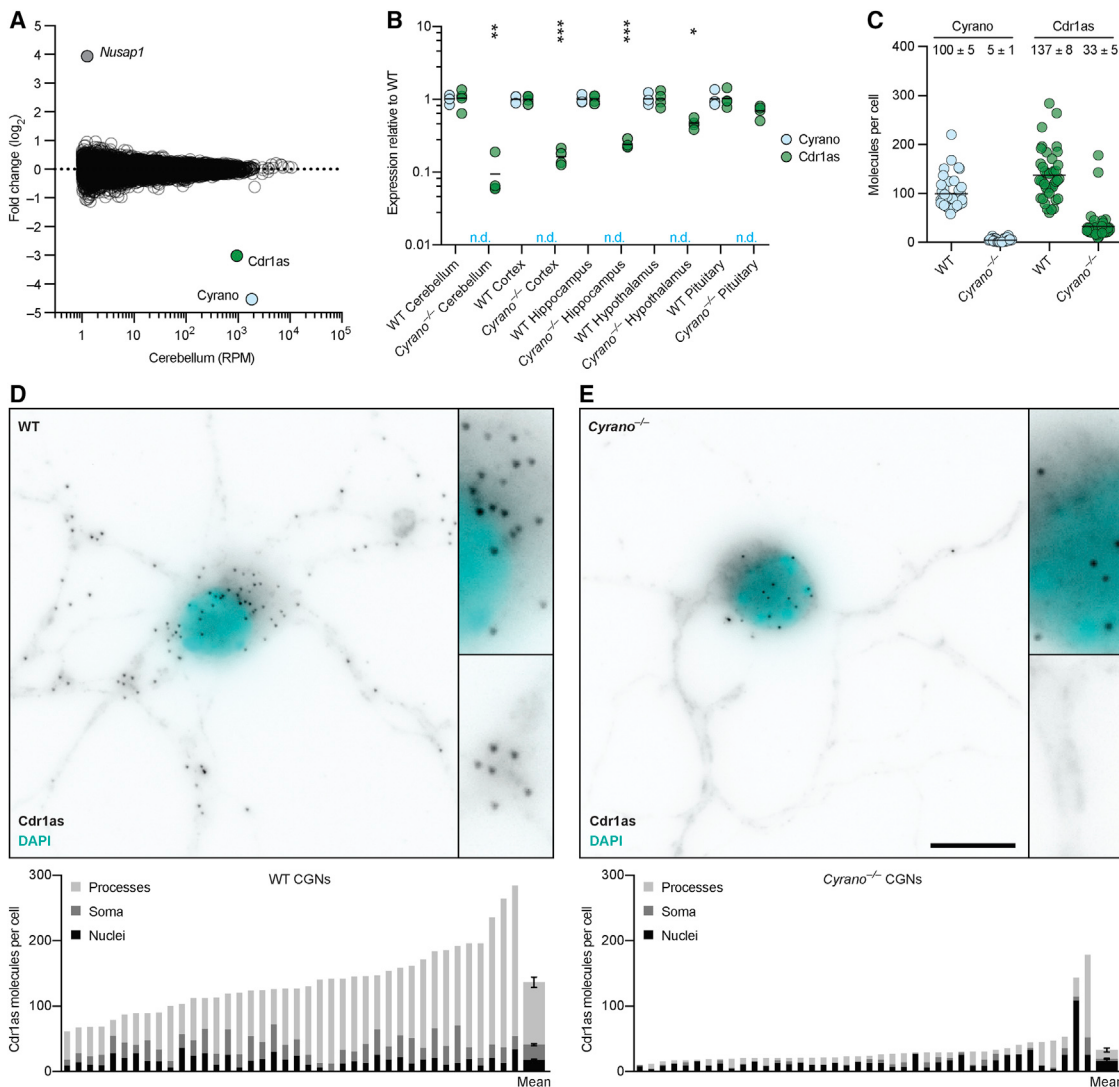


Figure 5. Cyrano Enables Cdr1as to Accumulate in the Brain

(A) Influence of Cyrano on RNA levels in cerebellum. Shown are fold changes in mean RNA levels observed between wild-type and *Cyrano*^{-/-} tissue (n = 4 per genotype), as determined by RNA-seq and plotted as a function of expression in wild-type tissue. Each circle represents a unique mRNA or noncoding RNA, showing results for all RNAs expressed above 1 RPM in wild-type tissue. Circles representing Cyrano, Cdr1as, and *Nusap1* are colored and labeled.

(B) Influence of Cyrano on Cdr1as expression in brain and pituitary. Levels of Cyrano (blue) and Cdr1as (green), as determined by RT-qPCR, were normalized to that of *Actb* and plotted relative to mean wild-type expression (black bars, mean; n = 4 per genotype; n.d., not detected). Statistically significant changes in Cdr1as levels in *Cyrano*^{-/-} tissues compared to wild-type tissues are indicated (*p < 0.05; **p < 0.01; ***p < 0.001, unpaired two-tailed t test).

(C) Influence of Cyrano on Cdr1as expression in DIV11 CGNs, as determined by single-molecule FISH. Plotted are the number of Cyrano and Cdr1as molecules per cell for wild-type and *Cyrano*^{-/-} CGNs. Each circle represents mean molecules per cell from a 100× microscopy field, each field containing 1–3 cells (n = 40 fields per genotype; black bars, mean). The mean of all fields for each genotype (± SEM) is also reported.

(D and E) Influence of Cyrano on accumulation of Cdr1as in neuronal cell bodies and processes. Shown is a representative image from single-molecule FISH experiments probing for Cdr1as in either wild-type (D) or *Cyrano*^{-/-} (E) CGNs, with insets showing increased magnification of a portion of soma and processes (Cdr1as, black; nuclei, cyan; scale bar, 10 μm). Below each image is quantification from the same 40 fields quantified in (C), with each bar reporting mean molecules per cell, differentiating molecules located in nuclei (black), soma (excluding nuclei, dark gray), and processes (light gray), plotting at the far right of each panel the means ± SEM.

See also Figure S5.

To test whether miR-7 is required for destabilization of Cdr1as in the absence of Cyrano, we generated mice that lacked both miR-7a1 and miR-7b, the two miR-7 paralogs most highly expressed in brain (Figure S6B). These *Mir7* double-knockout

(DKO) mice were born at the expected Mendelian frequency and had no gross abnormalities, despite a report that mice expressing a miR-7 sponge have smaller brains (Pollock et al., 2014) (Figure S6C; Table S1).

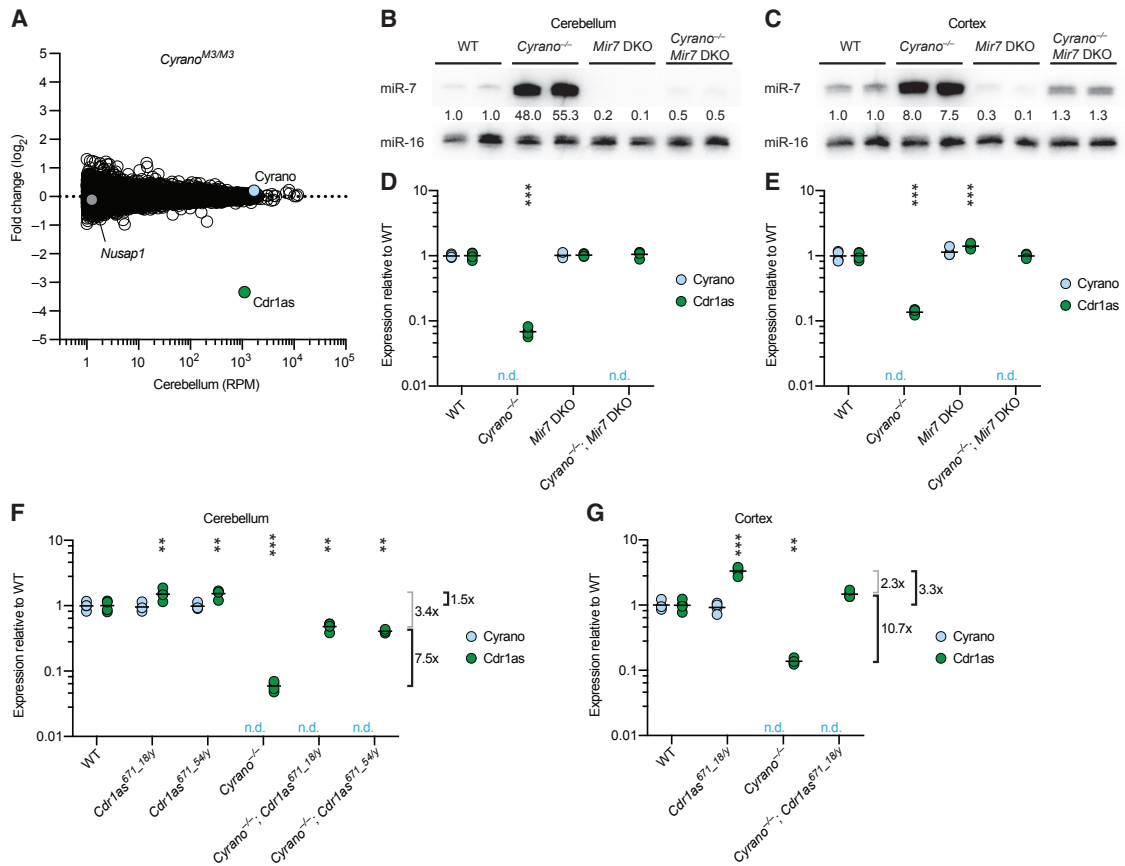


Figure 6. Cdr1as Is Regulated by miR-7 and miR-671

(A) Influence of the Cyrano miR-7 site on RNA levels in cerebellum. Shown are fold changes in mean RNA levels observed between wild-type and *Cyrano^{M3/M3}* cerebellum ($n = 3\text{--}4$ per genotype); otherwise, as in Figure 5A.

(B and C) Substantially reduced miR-7 levels in brains of *Mir7 DKO* mice. Shown are northern blots measuring miR-7 levels in cerebellum (B) and cortex (C) of mice with the indicated genotypes. Levels of miR-7 were normalized to those of miR-16 and are reported relative to the mean wild-type level.

(D and E) A requirement of miR-7 for Cdr1as reductions observed in mice without functional Cyrano. Levels of Cyrano (blue) and Cdr1as circRNA (green) in cerebellum (D) and cortex (E) of mice with the indicated genotypes were determined by qRT-PCR, normalized to *Actb*, and plotted relative to mean wild-type expression (black bars, mean; $n = 4$ per genotype; n.d., not detected). Statistical significance of the differences in Cdr1as level in each mutant tissue compared to that in wild-type tissue is indicated (** $p < 0.001$, ANOVA with Tukey's test).

(F and G) Influence of the miR-671 site within Cdr1as on Cdr1as levels both with and without functional Cyrano. Cyrano and Cdr1as in cerebellum (F) and cortex (G) of mice with the indicated genotypes were measured and plotted as in (D). Mean fold changes in Cdr1as attributable to the miR-671 site, either with or without functional Cyrano (thick brackets), and not attributable to the miR-671 site (thin brackets) are indicated to the right of each plot.

See also Figure S6 and Table S1.

Analysis of several brain regions showed that miR-7 levels substantially decreased throughout the brain of *Mir7 DKO* animals (Figures 6B, 6C, and S6D). Global analyses of predicted miR-7 targets revealed no significant changes in cerebellum and cortex, which indicated that the absolute levels of miR-7 normally found in these tissues were too low to direct detectable target repression (Figure S6E). When combining the *Cyrano* deletion with the *Mir7 DKO* to generate triple-knockout mice (*Cyrano^{-/-}; Mir7 DKO*), miR-7 levels, contributed by the third paralog (*Mir7a2*), did not substantially exceed that of wild-type mice (Figures 6B and 6C), thus providing a context in which *Cyrano* loss was no longer tied to abnormally high miR-7 levels. In this context, Cdr1as was insensitive to *Cyrano* loss, demonstrating that increased miR-7 levels were required for Cdr1as

destabilization in the absence of *Cyrano* (Figures 6D and 6E). Together, our results strongly supported a model in which *Cyrano*-directed miR-7 degradation protects Cdr1as from miR-7-mediated degradation, thereby allowing Cdr1as to accumulate in neuronal cell bodies and processes.

In the presence of *Cyrano*, Cdr1as levels were unaffected in *Mir7 DKO* cerebellum (Figures 6D and S6F), which indicated that in this region of the brain, *Cyrano*-mediated miR-7 degradation prevents miR-7 from detectably influencing Cdr1as levels. However, Cdr1as levels increased 1.4–2.3-fold in *Mir7 DKO* cortex, hippocampus, and hypothalamus (Figures 6E and S6F), indicating that in other regions, miR-7 reaches levels sufficient to influence Cdr1as accumulation even when *Cyrano* expression is intact.

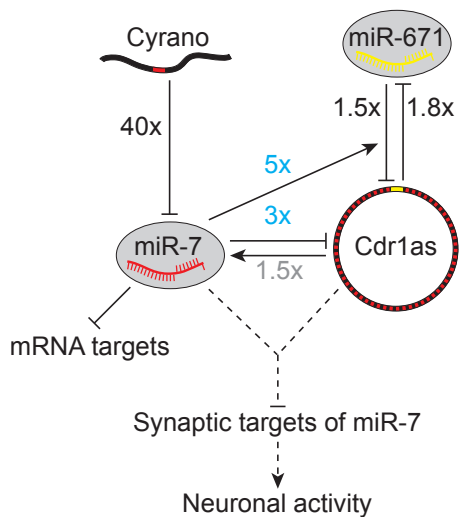


Figure 7. A Network of Noncoding Regulatory RNAs Acts in the Mammalian Brain

For each interaction, the effect was measured using a mouse-knockout model that disrupted either the relevant ncRNA (either Cyrano, miR-7, or Cdr1as) or miRNA-binding site (either the miR-7 site in Cyrano or the miR-671 site in Cdr1as). Fold changes are from the cerebellum, observed either in this study (black or blue) or previously (gray, Piwecka et al., 2017). The 1.8-fold increase in miR-671 observed in our mice with a disrupted Cdr1as miR-671 site resembled that observed in *Cdr1as*-knockout mice (Piwecka et al., 2017). Regulation that emerges with derepression of miR-7 in cerebellum (as opposed to deletion of miR-7) is indicated (blue fold changes). Repression of miR-7 targets is also depicted, but without a fold change because it was detected only in other tissues. Speculative interactions are shown as dashed lines.

In addition to many conserved miR-7 sites, Cdr1as also contains a single conserved miR-671 site, which pairs to the miRNA with complementarity sufficient to trigger Argonaute2-catalyzed slicing of the circRNA (Hansen et al., 2011). We hypothesized that miR-7-mediated degradation of Cdr1as might occur through enhanced miR-671-directed slicing. To be able to test this hypothesis, we generated mice with deletions (either 18 or 54 nt) that disrupted the miR-671 site (Figure S6G). Hemizygous males (*Cdr1as* is on the X chromosome) and homozygous females with either of these deletions were born at expected Mendelian frequencies, with no changes observed in miR-7 levels (Figure S6H; Table S1). Disruption of the miR-671 site within Cdr1as led to increased levels of Cdr1as in brain, up to 4-fold in cortex and hippocampus (Figure S6I). These results indicated that miR-671-directed slicing of Cdr1as, known to occur in cultured cells (Hansen et al., 2011), also occurs in the animal and is sufficiently robust to set Cdr1as levels in some brain regions.

With these *Cdr1as*⁶⁷¹ strains in hand, we generated *Cyrano*^{-/-}; *Cdr1as*^{671/y} mice and, after confirming that *Cyrano* deletion in the *Cdr1as*⁶⁷¹ background increased miR-7 levels (Figure S6J), we assessed Cdr1as expression. If enhanced miR-671-directed slicing was fully responsible for Cdr1as clearance in *Cyrano*^{-/-} mice, Cdr1as expression in *Cyrano*^{-/-}; *Cdr1as*^{671/y} mice was expected to increase to the same level as that of *Cdr1as*^{671/y} mice,

whereas if enhanced slicing was not involved, Cdr1as was expected to increase relative to the *Cyrano*^{-/-} by a fold change similar to that observed between wild-type and *Cdr1as*^{671/y} mice (1.5- and 3.3-fold in cerebellum and cortex, respectively). Instead of either of these extremes, we observed that Cdr1as levels were partially restored. In cerebellum, Cdr1as increased 7.5-fold, implying a 5-fold (7.5 ÷ 1.5) increase in slicing at the miR-671 site in the absence of *Cyrano* activity (Figure 6F). The observation that preventing miR-671-directed slicing only partially restored Cdr1as levels indicated that at least one other miR-7-dependent mechanism acts to degrade Cdr1as in this tissue, with a presumed 3.4-fold effect. Likewise, in cortex, Cdr1as increased 10.7-fold, implying a 3.2-fold (10.7 ÷ 3.3) increase in slicing at the miR-671 site, with another 2.3-fold attributed to another mechanism (Figure 6G). Taken together, our results showed that in the absence of *Cyrano*-directed miR-7 degradation, miR-7 levels in brain tissues increase such that miR-7 destroys Cdr1as through at least two mechanisms, one of which increases slicing at the miR-671 site.

DISCUSSION

We characterize a posttranscriptional regulatory network centered on four noncoding RNAs—one lncRNA, one circRNA, and two miRNAs—using a panel of mouse knockouts to disrupt nodes and edges in the network and thereby learn their molecular consequences in the animal (Figure 7). The lncRNA *Cyrano* functions as a potent miR-7 assassin. In targeting miR-7 for degradation, *Cyrano* prevents miR-7 from repressing its mRNA targets in some tissues. *Cyrano* also prevents miR-7 from causing efficient cytoplasmic destruction of the circRNA Cdr1as in the brain, which occurs in part by enhancing miR-671-directed slicing of Cdr1as.

Insights into TDMD

Cyrano-targeted miR-7 destruction is surprisingly potent compared to previously described TDMD examples. Although a highly complementary miRNA-binding site is required to induce TDMD (Ameres et al., 2010), additional sequences within the full-length RNA can augment the activity (Lee et al., 2013). *Cyrano* is substantially longer than viral transcripts that direct miRNA degradation and has deeply conserved blocks of sequence proximal to the miR-7 site and elsewhere within the transcript (Ulitsky et al., 2011) (Figure 1A). Consistent with these more distal conserved regions potentially enhancing *Cyrano*-directed miR-7 degradation, we observed only a 3-fold decrease in miR-7 after >100-fold overexpression of the 197 nt site-containing region of *Cyrano* (Figure 2D). This strategy of using multiple regions of a lncRNA to boost degradation efficacy would be suitable for an endogenous transcript, whereas the pressure to minimize genome size might favor the viral strategy of using a larger number of shorter, less effective transcripts.

Thus far, the miRNA-degradation factors responsible for TDMD have been elusive. As tailing and trimming of miRNA 3' ends co-occur with TDMD, an attractive model has been that tailing of the 3' end of the miRNA licenses the miRNA for degradation by a 3'-to-5' exonuclease. This model is consistent with findings that (1) 2'-O-methylation, a modification that both

prevents 3' tailing and stabilizes small RNAs, is typically found on classes of small regulatory RNAs that have extensive pairing to most targets yet is absent on metazoan miRNAs, which do not have extensive pairing to most targets (Ameres et al., 2010; Ji and Chen, 2012); (2) tailing of certain metazoan miRNAs and pre-miRNAs promotes their destruction (Boele et al., 2014; Chang et al., 2013; Katoh et al., 2015); and (3) nucleotidyltransferases and 3'-to-5' exonucleases co-purify and cooperate in protein complexes (Kim and Richter, 2006; Reimão-Pinto et al., 2016). Despite the appeal of this model, our findings comparing *Cyrano*^{-/-} and *Gld2*^{-/-} mice indicated that the observed tailing is off-pathway for degradation, in which case, trimming might also be an off-pathway event caused by transiently freeing the 3' end of the miRNA from Argonaute. In this scenario, TDMD need not occur through a 3'-to-5' exonuclease. Indeed, severe knockdown of candidate 3'-to-5' exonucleases had no detectable effect on *Cyrano*-directed miR-7 degradation (Figures S4H and S4I). Although we have not ruled out redundancy or a role for other cytoplasmic exonucleases, perhaps the key factors recruited by *Cyrano* are not nucleases at all but instead act on Argonaute to either degrade the protein or help eject *Cyrano*-bound miR-7. Once removed from the protective grip of Argonaute, miR-7 could be destroyed by multiple cellular nucleases. Alternatively, *Cyrano* might induce a transient tailing of miR-7 that was not detected in our analyses because it was coupled to rapid, highly processive miRNA degradation. The discovery of the unusually effective TDMD mediated by *Cyrano* provides a promising system for dissection of this phenomenon.

Destruction of a circRNA

circRNAs are much more stable than mRNAs, presumably due to the absence of free ends (Ebbesen et al., 2017). *Cdr1as* is unusual in that it has a built-in mechanism for destruction via miR-671-directed slicing. We found that this mechanism is active in the animal, controlling accumulation of *Cdr1as* in brain. In *Cyrano*^{-/-} brains, miR-671-directed slicing of *Cdr1as* is further enhanced due to increased levels of miR-7. Perhaps miR-7, which has sites in close proximity to the miR-671 site, helps recruit or retain the miR-671 silencing complex through an undefined mechanism that also explains the cooperative action of closely spaced sites in mediating repression (Grimson et al., 2007; Saetrom et al., 2007). For example, the miR-7 and miR-671 silencing complexes might cooperatively bind to *Cdr1as*, or binding of miR-7 to *Cdr1as* might change the conformation of *Cdr1as* so as to increase accessibility of the miR-671 site.

Increased miR-671-directed slicing explains 3–5-fold of the *Cdr1as* degradation observed in *Cyrano*^{-/-} cerebellum and cortex; at least one other miR-7-dependent mechanism is responsible for the remaining 2–3-fold. miR-7 is not expected to direct slicing of *Cdr1as* by Argonaute2 because *Cdr1as* has no site with extensive complementarity to miR-7. Perhaps *Cdr1as* studded with too many Argonautes is trafficked to a more degradative subcellular environment.

A Network of Noncoding RNAs Acting in Neurons

What might be the purpose of this baroque regulatory network centered on four noncoding RNAs? With its unusually high number of miR-7 sites, *Cdr1as* was initially proposed to act as

a miR-7 inhibitor, titrating miR-7 away from mRNA targets while resisting deadenylation and decapping typically induced by stable Argonaute binding (Hansen et al., 2013; Memczak et al., 2013). Although this proposal has gained popularity, there is no evidence that endogenous *Cdr1as* acts as a sponge. Knocking out *Cdr1as* does not lead to the decreased levels of miR-7 targets expected if *Cdr1as* were a miR-7 sponge (Piwecka et al., 2017). Instead, the role of *Cdr1as* in dampening neuronal activity is partly attributed to the idea that it protects miR-7 from degradation, thereby allowing increased repression of miR-7 targets (Piwecka et al., 2017).

One concern with this more recent idea is the small effect size observed for predicted miR-7 targets in *Cdr1as*-knockout tissues (Piwecka et al., 2017). Furthermore, the results of our experiments are difficult to reconcile with the notion that the ≤ 2 -fold decrease in miR-7 observed in the *Cdr1as* knockout helps explain this knockout phenotype; when examining the effects of decreased miR-7 levels (>5 -fold) in the *Mir7* double knockout, we found no evidence for decreased repression of miR-7 targets in regions of the brain where *Cdr1as* is thought to be active (Figure S6E).

So how else might *Cdr1as* function to dampen neuronal activity? Although we do not favor the idea that its influence on miR-7 levels is at the heart of its function, the observation of its activity in tissues in which miR-7 levels seem too low to have any consequence on its general target repertoire imply that *Cdr1as* might potentiate miR-7 activity in some other way. We favor the proposal that *Cdr1as* acts to engineer spatial and perhaps temporal delivery of miR-7 in neurons (Piwecka et al., 2017). Controlled delivery of miR-7 to synapses might limit neuronal activity without detectable effects on most miR-7 targets. This idea is consistent with the observation that miR-7 has multiple conserved targets involved in vesicle trafficking (Latreille et al., 2014) and reports of miR-7 enrichment in neuronal processes (Siegel et al., 2009; Smalheiser et al., 2014). That *Cdr1as* contains sites for miR-7 instead of another lowly expressed neuronal miRNA suggests that what might matter is not merely the low expression of miR-7 but also its potent on-off switch in the form of *Cyrano*-directed degradation. Our insights regarding the crosstalk and molecular consequences of these noncoding RNAs, together with our knockout models disrupting nodes and edges of the network, help lay the foundation for experimental tests of these ideas.

STAR★METHODS

Detailed methods are provided in the online version of this paper and include the following:

- KEY RESOURCES TABLE
- CONTACT FOR REAGENT AND RESOURCE SHARING
- EXPERIMENTAL MODEL AND SUBJECT DETAILS
 - Mouse husbandry
 - Generation of *Cyrano*^{fl/fl} and *Cyrano*^{-/-} mice
 - Generation of mutant mice using Cas9
 - Genotyping
 - Cell lines and cell culture
 - CRISPRi-based knockdown cell lines

- Primary neuronal cultures
- **METHOD DETAILS**
 - RNA extraction
 - Cytoplasmic/nuclear fractionation
 - Lentivirus production and transduction
 - RNA-seq
 - Small-RNA sequencing
 - Northern blots
 - RT-qPCR
 - Absolute quantification of miR-7, Cyrano, and Cdr1as in CGNs and cell lines
 - Single-molecule FISH
- **QUANTIFICATION AND STATISTICAL ANALYSIS**
- **DATA AND SOFTWARE AVAILABILITY**

SUPPLEMENTAL INFORMATION

Supplemental Information includes six figures and three tables and can be found with this article online at <https://doi.org/10.1016/j.cell.2018.05.022>.

ACKNOWLEDGMENTS

We thank E. Kingston, A. Shkumatava, I. Ulitsky, other current and former members of the Bartel lab, M. Piwecka, N. Rajewsky, and A. Granger for helpful discussions; A. Liu for technical assistance; T. Eisen for hippocampal cultures; S. Eichhorn, J. Kwasnieski, K. Lin, J. Morgan, and X. Wu for computational advice; the Whitehead Institute Genome Technology Core for sequencing; W. Salmon and the Keck Imaging Facility for microscopy expertise; the Janelia Gene Targeting and Transgenic Facility, the MIT Transgenic Facility, and the Whitehead Institute Genetically Engineered Models Facility for generating mutant mice. This research was supported by NIH grants GM061835 and GM118135 (D.P.B.) and T32CA009216 (B.K.). D.P.B. is an investigator of the Howard Hughes Medical Institute.

AUTHOR CONTRIBUTIONS

B.K. and D.P.B. conceived the project and designed the study. B.K. performed all of the experiments, with contributions from J.S., except for the CRISPRi experiments, which were performed and analyzed by C.Y.S. B.K. performed all other analyses and drafted the manuscript. B.K., C.Y.S., and D.P.B revised the manuscript.

DECLARATION OF INTERESTS

The authors declare no competing interests.

Received: February 9, 2018

Revised: March 23, 2018

Accepted: May 10, 2018

Published: June 7, 2018

REFERENCES

- Agarwal, V., Bell, G.W., Nam, J.W., and Bartel, D.P. (2015). Predicting effective microRNA target sites in mammalian mRNAs. *eLife* 4, e05005.
- Ahmed, K., LaPierre, M.P., Gasser, E., Denzler, R., Yang, Y., Rülicke, T., Kero, J., Latreille, M., and Stoffel, M. (2017). Loss of microRNA-7a2 induces hypogonadotropic hypogonadism and infertility. *J. Clin. Invest.* 127, 1061–1074.
- Ameres, S.L., Horwich, M.D., Hung, J.H., Xu, J., Ghildiyal, M., Weng, Z., and Zamore, P.D. (2010). Target RNA-directed trimming and tailing of small silencing RNAs. *Science* 328, 1534–1539.
- Ameres, S.L., Hung, J.H., Xu, J., Weng, Z., and Zamore, P.D. (2011). Target RNA-directed tailing and trimming purifies the sorting of endo-siRNAs between the two Drosophila Argonaute proteins. *RNA* 17, 54–63.
- Anders, S., Pyl, P.T., and Huber, W. (2015). HTSeq—a Python framework to work with high-throughput sequencing data. *Bioinformatics* 31, 166–169.
- Avraham, R., Sas-Chen, A., Manor, O., Steinfeld, I., Shalgi, R., Tarcic, G., Bonsel, N., Zeisel, A., Amit, I., Zwang, Y., et al. (2010). EGF decreases the abundance of microRNAs that restrain oncogenic transcription factors. *Sci. Signal.* 3, ra43.
- Baccarini, A., Chauhan, H., Gardner, T.J., Jayaprakash, A.D., Sachidanandam, R., and Brown, B.D. (2011). Kinetic analysis reveals the fate of a microRNA following target regulation in mammalian cells. *Curr. Biol.* 21, 369–376.
- Bail, S., Swerdlow, M., Liu, H., Jiao, X., Goff, L.A., Hart, R.P., and Kiledjian, M. (2010). Differential regulation of microRNA stability. *RNA* 16, 1032–1039.
- Barrett, S.P., Parker, K.R., Horn, C., Mata, M., and Salzman, J. (2017). ciRS-7 exonic sequence is embedded in a long non-coding RNA locus. *PLOS Genetics* 13, e1007114.
- Bartel, D.P. (2018). Metazoan MicroRNAs. *Cell* 173, 20–51.
- Batish, M., Raj, A., and Tyagi, S. (2011). Single molecule imaging of RNA in situ. *Methods Mol. Biol.* 714, 3–13.
- Beaudoin, G.M., 3rd, Lee, S.H., Singh, D., Yuan, Y., Ng, Y.G., Reichardt, L.F., and Arikath, J. (2012). Culturing pyramidal neurons from the early postnatal mouse hippocampus and cortex. *Nat. Protoc.* 7, 1741–1754.
- Bitetti, A., Mallory, A.C., Golini, E., Carrieri, C., Carreño Gutiérrez, H., Perlas, E., Pérez-Rico, Y.A., Tocchini-Valentini, G.P., Enright, A.J., Norton, W.H.J., et al. (2018). MicroRNA degradation by a conserved target RNA regulates animal behavior. *Nat. Struct. Mol. Biol.* 25, 244–251.
- Boele, J., Persson, H., Shin, J.W., Ishizu, Y., Newie, I.S., Søkilde, R., Hawkins, S.M., Coarfa, C., Ikeda, K., Takayama, K., et al. (2014). PAPD5-mediated 3'adenylation and subsequent degradation of miR-21 is disrupted in proliferative disease. *Proc. Natl. Acad. Sci. USA* 111, 11467–11472.
- Cazalla, D., Yario, T., and Steitz, J.A. (2010). Down-regulation of a host microRNA by a Herpesvirus saimiri noncoding RNA. *Science* 328, 1563–1566.
- Chang, H.M., Triboulet, R., Thornton, J.E., and Gregory, R.I. (2013). A role for the Perlman syndrome exonuclease Dis3l2 in the Lin28-let-7 pathway. *Nature* 497, 244–248.
- de la Mata, M., Gaidatzis, D., Vitanescu, M., Stadler, M.B., Wentzel, C., Scheifele, P., Filipowicz, W., and Großhans, H. (2015). Potent degradation of neuronal miRNAs induced by highly complementary targets. *EMBO Rep.* 16, 500–511.
- Denzler, R., McGeary, S.E., Title, A.C., Agarwal, V., Bartel, D.P., and Stoffel, M. (2016). Impact of microRNA levels, target-site complementarity, and cooperativity on competing endogenous RNA-regulated gene expression. *Mol. Cell* 64, 565–579.
- Dobin, A., Davis, C.A., Schlesinger, F., Drenkow, J., Zaleski, C., Jha, S., Batut, P., Chaisson, M., and Gingeras, T.R. (2013). STAR: ultrafast universal RNA-seq aligner. *Bioinformatics* 29, 15–21.
- Dong, X., Chen, K., Cuevas-Diaz Duran, R., You, Y., Sloan, S.A., Zhang, Y., Zong, S., Cao, Q., Barres, B.A., and Wu, J.Q. (2015). Comprehensive identification of long non-coding RNAs in purified cell types from the brain reveals functional lncRNA in OPC fate determination. *PLoS Genet.* 11, e1005669.
- Duffy, E.E., Rutenberg-Schoenberg, M., Stark, C.D., Kitchen, R.R., Gerstein, M.B., and Simon, M.D. (2015). Tracking distinct RNA populations using efficient and reversible covalent chemistry. *Mol. Cell* 59, 858–866.
- Ebbesen, K.K., Hansen, T.B., and Kjems, J. (2017). Insights into circular RNA biology. *RNA Biol.* 14, 1035–1045.
- Eichhorn, S.W., Guo, H., McGeary, S.E., Rodriguez-Mias, R.A., Shin, C., Baek, D., Hsu, S.H., Ghoshal, K., Villén, J., and Bartel, D.P. (2014). mRNA destabilization is the dominant effect of mammalian microRNAs by the time substantial repression ensues. *Mol. Cell* 56, 104–115.
- Elbashir, S.M., Martinez, J., Patkaniowska, A., Lendeckel, W., and Tuschl, T. (2001). Functional anatomy of siRNAs for mediating efficient RNAi in *Drosophila melanogaster* embryo lysate. *EMBO J.* 20, 6877–6888.

- Fang, W., and Bartel, D.P. (2015). The menu of features that define primary microRNAs and enable de novo design of microRNA genes. *Mol. Cell* 60, 131–145.
- Gantier, M.P., McCoy, C.E., Rusinova, I., Saulep, D., Wang, D., Xu, D., Irving, A.T., Behlke, M.A., Hertzog, P.J., Mackay, F., and Williams, B.R. (2011). Analysis of microRNA turnover in mammalian cells following Dicer1 ablation. *Nucleic Acids Res.* 39, 5692–5703.
- Gilbert, L.A., Horlbeck, M.A., Adamson, B., Villalta, J.E., Chen, Y., Whitehead, E.H., Guimaraes, C., Panning, B., Ploegh, H.L., Bassik, M.C., et al. (2014). Genome-scale CRISPR-mediated control of gene repression and activation. *Cell* 159, 647–661.
- Gilbert, L.A., Larson, M.H., Morsut, L., Liu, Z., Brar, G.A., Torres, S.E., Stern-Ginossar, N., Brandman, O., Whitehead, E.H., Doudna, J.A., et al. (2013). CRISPR-mediated modular RNA-guided regulation of transcription in eukaryotes. *Cell* 154, 442–451.
- Grimson, A., Farh, K.K., Johnston, W.K., Garrett-Engle, P., Lim, L.P., and Bartel, D.P. (2007). MicroRNA targeting specificity in mammals: determinants beyond seed pairing. *Mol. Cell* 27, 91–105.
- Guo, Y., Liu, J., Elfenbein, S.J., Ma, Y., Zhong, M., Qiu, C., Ding, Y., and Lu, J. (2015). Characterization of the mammalian miRNA turnover landscape. *Nucleic Acids Res.* 43, 2326–2341.
- Haas, G., Cetin, S., Messmer, M., Chane-Woon-Ming, B., Terenzi, O., Chicher, J., Kuhn, L., Hammann, P., and Pfeffer, S. (2016). Identification of factors involved in target RNA-directed microRNA degradation. *Nucleic Acids Res.* 44, 2873–2887.
- Hansen, T.B., Jensen, T.I., Clausen, B.H., Bramsen, J.B., Finsen, B., Damgaard, C.K., and Kjems, J. (2013). Natural RNA circles function as efficient microRNA sponges. *Nature* 495, 384–388.
- Hansen, T.B., Wiklund, E.D., Bramsen, J.B., Villadsen, S.B., Statham, A.L., Clark, S.J., and Kjems, J. (2011). miRNA-dependent gene silencing involving Ago2-mediated cleavage of a circular antisense RNA. *EMBO J.* 30, 4414–4422.
- Hoch, R.V., and Soriano, P. (2006). Context-specific requirements for Fgf1 signaling through Frs2 and Frs3 during mouse development. *Development* 133, 663–673.
- Hwang, H.W., Wentzel, E.A., and Mendell, J.T. (2007). A hexanucleotide element directs microRNA nuclear import. *Science* 315, 97–100.
- Ji, L., and Chen, X. (2012). Regulation of small RNA stability: methylation and beyond. *Cell Res.* 22, 624–636.
- Jonas, S., and Izaurralde, E. (2015). Towards a molecular understanding of microRNA-mediated gene silencing. *Nat. Rev. Genet.* 16, 421–433.
- Katoh, T., Hojo, H., and Suzuki, T. (2015). Destabilization of microRNAs in human cells by 3' deadenylation mediated by PARN and CUGBP1. *Nucleic Acids Res.* 43, 7521–7534.
- Katoh, T., Sakaguchi, Y., Miyauchi, K., Suzuki, T., Kashiwabara, S., Baba, T., and Suzuki, T. (2009). Selective stabilization of mammalian microRNAs by 3' adenylation mediated by the cytoplasmic poly(A) polymerase GLD-2. *Genes Dev.* 23, 433–438.
- Kim, J.H., and Richter, J.D. (2006). Opposing polymerase-deadenylase activities regulate cytoplasmic polyadenylation. *Mol. Cell* 24, 173–183.
- Kok, F.O., Shin, M., Ni, C.W., Gupta, A., Grosse, A.S., van Impel, A., Kirchmair, B.C., Peterson-Maduro, J., Kourkoulis, G., Male, I., et al. (2015). Reverse genetic screening reveals poor correlation between morpholino-induced and mutant phenotypes in zebrafish. *Dev. Cell* 32, 97–108.
- Kopp, F., and Mendell, J.T. (2018). Functional classification and experimental dissection of long noncoding RNAs. *Cell* 172, 393–407.
- Krol, J., Busskamp, V., Markiewicz, I., Stadler, M.B., Ribi, S., Richter, J., Duebel, J., Bicker, S., Fehling, H.J., Schübel, D., et al. (2010). Characterizing light-regulated retinal microRNAs reveals rapid turnover as a common property of neuronal microRNAs. *Cell* 141, 618–631.
- Latreille, M., Hausser, J., Stützer, I., Zhang, Q., Hastoy, B., Gargani, S., Kerr-Conte, J., Pattou, F., Zavolan, M., Esguerra, J.L., et al. (2014). MicroRNA-7a regulates pancreatic β cell function. *J. Clin. Invest.* 124, 2722–2735.
- Lee, H.Y., Greene, L.A., Mason, C.A., and Manzini, M.C. (2009). Isolation and culture of post-natal mouse cerebellar granule neuron progenitor cells and neurons. *J. Vis. Exp.* (23), e990.
- Lee, S., Song, J., Kim, S., Kim, J., Hong, Y., Kim, Y., Kim, D., Baek, D., and Ahn, K. (2013). Selective degradation of host MicroRNAs by an intergenic HCMV noncoding RNA accelerates virus production. *Cell Host Microbe* 13, 678–690.
- Lee, S.I., Murthy, S.C., Trimble, J.J., Desrosiers, R.C., and Steitz, J.A. (1988). Four novel U RNAs are encoded by a herpesvirus. *Cell* 54, 599–607.
- Lein, E.S., Hawrylycz, M.J., Ao, N., Ayres, M., Bensinger, A., Bernard, A., Boe, A.F., Boguski, M.S., Brockway, K.S., Byrnes, E.J., et al. (2007). Genome-wide atlas of gene expression in the adult mouse brain. *Nature* 445, 168–176.
- Libri, V., Helwak, A., Miesen, P., Santhakumar, D., Borger, J.G., Kudla, G., Grey, F., Tollervey, D., and Buck, A.H. (2012). Murine cytomegalovirus encodes a miR-27 inhibitor disguised as a target. *Proc. Natl. Acad. Sci. USA* 109, 279–284.
- Love, M.I., Huber, W., and Anders, S. (2014). Moderated estimation of fold change and dispersion for RNA-seq data with DESeq2. *Genome Biol.* 15, 550.
- Lyubimova, A., Itzkovitz, S., Junker, J.P., Fan, Z.P., Wu, X., and van Oudenaarden, A. (2013). Single-molecule mRNA detection and counting in mammalian tissue. *Nat. Protoc.* 8, 1743–1758.
- Mansur, F., Ivshina, M., Gu, W., Schaevitz, L., Stackpole, E., Guija, S., Edwards, Y.J., and Richter, J.D. (2016). Gld2-catalyzed 3' monoadenylation of miRNAs in the hippocampus has no detectable effect on their stability or on animal behavior. *RNA* 22, 1492–1499.
- Marcinowski, L., Tanguy, M., Krmpotic, A., Rädle, B., Lisnić, V.J., Tuddenham, L., Chane-Woon-Ming, B., Ruzsics, Z., Erhard, F., Benkartek, C., et al. (2012). Degradation of cellular mir-27 by a novel, highly abundant viral transcript is important for efficient virus replication in vivo. *PLoS Pathog.* 8, e1002510.
- Martin, M. (2011). Cutadapt removes adapter sequences from high-throughput sequencing reads. *EMBnet.journal* 17, 10–12.
- Memczak, S., Jens, M., Elefsinioti, A., Torti, F., Krueger, J., Rybak, A., Maier, L., Mackowiak, S.D., Gregersen, L.H., Munschauer, M., et al. (2013). Circular RNAs are a large class of animal RNAs with regulatory potency. *Nature* 495, 333–338.
- Piwecka, M., Glażar, P., Hernandez-Miranda, L.R., Memczak, S., Wolf, S.A., Rybak-Wolf, A., Filipchuk, A., Kliromos, F., Cerda Jara, C.A., Fenske, P., et al. (2017). Loss of a mammalian circular RNA locus causes miRNA deregulation and affects brain function. *Science* 357, eaam8526.
- Pollard, K.S., Hubisz, M.J., Rosenbloom, K.R., and Siepel, A. (2010). Detection of nonneutral substitution rates on mammalian phylogenies. *Genome Res.* 20, 110–121.
- Pollock, A., Bian, S., Zhang, C., Chen, Z., and Sun, T. (2014). Growth of the developing cerebral cortex is controlled by microRNA-7 through the p53 pathway. *Cell Rep.* 7, 1184–1196.
- Reimão-Pinto, M.M., Manzenreither, R.A., Burkard, T.R., Sledz, P., Jinek, M., Mechtl, K., and Ameres, S.L. (2016). Molecular basis for cytoplasmic RNA surveillance by uridylation-triggered decay in *Drosophila*. *EMBO J.* 35, 2417–2434.
- Rissland, O.S., Hong, S.J., and Bartel, D.P. (2011). MicroRNA destabilization enables dynamic regulation of the miR-16 family in response to cell-cycle changes. *Mol. Cell* 43, 993–1004.
- Saetrom, P., Heale, B.S., Snøve, O., Jr., Aagaard, L., Alluin, J., and Rossi, J.J. (2007). Distance constraints between microRNA target sites dictate efficacy and cooperativity. *Nucleic Acids Res.* 35, 2333–2342.
- Siegel, G., Obernosterer, G., Fiore, R., Oehmen, M., Bicker, S., Christensen, M., Khudayberdiev, S., Leuschner, P.F., Busch, C.J., Kane, C., et al. (2009). A functional screen implicates microRNA-138-dependent regulation of the de-palmitoylation enzyme APT1 in dendritic spine morphogenesis. *Nat. Cell Biol.* 11, 705–716.

- Siepel, A., Bejerano, G., Pedersen, J.S., Hinrichs, A.S., Hou, M., Rosenbloom, K., Clawson, H., Spieth, J., Hillier, L.W., Richards, S., et al. (2005). Evolutionarily conserved elements in vertebrate, insect, worm, and yeast genomes. *Genome Res.* 15, 1034–1050.
- Smalheiser, N.R., Lugli, G., Zhang, H., Rizavi, H., Cook, E.H., and Dwivedi, Y. (2014). Expression of microRNAs and other small RNAs in prefrontal cortex in schizophrenia, bipolar disorder and depressed subjects. *PLoS ONE* 9, e86469.
- Thorvaldsdóttir, H., Robinson, J.T., and Mesirov, J.P. (2013). Integrative Genomics Viewer (IGV): high-performance genomics data visualization and exploration. *Brief. Bioinform.* 14, 178–192.
- Truett, G.E., Heeger, P., Mynatt, R.L., Truett, A.A., Walker, J.A., and Warman, M.L. (2000). Preparation of PCR-quality mouse genomic DNA with hot sodium hydroxide and tris (HotSHOT). *BioTechniques* 29, 52–54.
- Ulitsky, I., Shkumatava, A., Jan, C.H., Sive, H., and Bartel, D.P. (2011). Conserved function of lncRNAs in vertebrate embryonic development despite rapid sequence evolution. *Cell* 147, 1537–1550.
- Visel, A., Thaller, C., and Eichele, G. (2004). GenePaint.org: an atlas of gene expression patterns in the mouse embryo. *Nucleic Acids Res.* 32, D552–D556.
- Xie, J., Ameres, S.L., Friedline, R., Hung, J.H., Zhang, Y., Xie, Q., Zhong, L., Su, Q., He, R., Li, M., et al. (2012). Long-term, efficient inhibition of microRNA function in mice using rAAV vectors. *Nat. Methods* 9, 403–409.

STAR★METHODS

KEY RESOURCES TABLE

REAGENT or RESOURCE	SOURCE	IDENTIFIER
Antibodies		
Mouse monoclonal anti-MAP2, clone ap20	Millipore	RRID: AB_94856
Guinea pig polyclonal anti-Tau	Synaptic Systems	RRID: AB_1547385
Rabbit polyclonal anti-GFAP	Dako	RRID: AB_10013382
Bacterial and Virus Strains		
One Shot TOP10 chemically competent <i>E. coli</i>	Life Technologies	C404006
Chemicals, Peptides, and Recombinant Proteins		
[γ - ³² P]ATP	PerkinElmer	NEG035C001MC
TRI Reagent Solution	Life Technologies	AM9738
Chloroform	J.T. Baker Analytical	9180-01
Yeast tRNA	Life Technologies	15401011
Superase-In	Life Technologies	AM2696
GE Healthcare Hybond-NX Membrane	VWR	95038-412
ULTRAhyb-Oligo hybridization buffer	Life Technologies	AM8663
EDC (<i>N</i> -(3-dimethylaminopropyl)- <i>N'</i> -ethylcarbodiimide)	Thermo Scientific	22891
Spin-X Centrifuge Tube Filters	Corning	CLS8162
Critical Commercial Assays		
TruSeq unstranded RNA Library kit	Illumina	RS-122-2001
NEXTflex stranded RNA-seq kit	Bioo Scientific	5138-10
Lipofectamine 2000	Life Technologies	11668019
QuikChange Lightning Multi Site-Directed Mutagenesis	Agilent	210515
KAPA HiFi HotStart ReadyMix	Roche	KK2601
KAPA 2G Fast Genotyping Mix	Roche	KK5121
Papain Dissociation System	Worthington	LK003150
Micro Bio-Spin P30 gel columns	Bio-Rad	7326250
QuantiTect RT kit	QIAGEN	205311
Turbo DNase	Life Technologies	AM2239
RQ1 DNase	Promega	M6101
T4 PNK	New England Biolabs	101228-172
SuperScript III Reverse Transcriptase	Life Technologies	18080044
SYBR Green PCR Master Mix	Applied Biosystems	4309155
Deposited Data		
RNA-seq	This paper	GEO: GSE112635
Small-RNA sequencing	This paper	GEO: GSE112635
<i>Mir7a2</i> ^{-/-} pituitary RNA-seq	Ahmed et al., 2017	ENA PRJEB12612
<i>Gld2</i> ^{-/-} hippocampus RNA-seq	Mansur et al., 2016	GEO: GSE114259
Experimental Models: Cell Lines		
Human: K562-dCas9-KRAB	Gilbert et al., 2014	N/A
Human: HEK293T	ATCC	CRL-3216
Human: HEK293	ATCC	CRL-1573
Human: HeLa	ATCC	CCL-2
Human: SH-SY5Y	ATCC	CRL-2266
Human: MCF7	ATCC	HTB-22
Human: SK-N-SH	ATCC	HTB-11

(Continued on next page)

Continued

REAGENT or RESOURCE	SOURCE	IDENTIFIER
Mouse: Neuro2a	ATCC	CCL-131
Mouse: C2C12	ATCC	CRL-1772
Human: HeLa-dCas9-BFP-KRAB	This paper	N/A
Human: SH-SY5Y-dCas9-BFP-KRAB	This paper	N/A
Human: MCF7-dCas9-BFP-KRAB	This paper	N/A
Human: SK-N-SH-dCas9-BFP-KRAB	This paper	N/A
Mouse: C2C12-dCas9-BFP-KRAB	This paper	N/A
Experimental Models: Organisms/Strains		
Mouse: <i>Cyrano</i> ^{fl/fl}	This paper	N/A
Mouse: <i>Cyrano</i> ^{-/-}	This paper	N/A
Mouse: <i>Cyrano</i> ^{M1/M1}	This paper	N/A
Mouse: <i>Cyrano</i> ^{M2/M2}	This paper	N/A
Mouse: <i>Cyrano</i> ^{M3/M3}	This paper	N/A
Mouse: <i>Cyrano</i> ^{M4/M4}	This paper	N/A
Mouse: <i>Cyrano</i> ^{M5/M5}	This paper	N/A
Mouse: <i>Cyrano</i> ^{M6/M6}	This paper	N/A
Mouse: <i>Mir7a1</i> ^{-/-} ; <i>Mir7b</i> ^{-/-}	This paper	N/A
Mouse: <i>Cdr1as</i> ^{671_18/y}	This paper	N/A
Mouse: <i>Cdr1as</i> ^{671_54/y}	This paper	N/A
Oligonucleotides		
See Table S3	This paper	N/A
Single-molecule FISH probes (also listed in Table S3)	Biosearch Technologies	SMF-1065-5
miR-7 LNA northern probe	Exiqon	38485-00
Recombinant DNA		
pPGKneoF2L2DTA	Hoch and Soriano, 2006	Addgene #13445
pHR-SFFV-dCas9-BFP-KRAB	Gilbert et al., 2013	Addgene #46911
pU6-sgRNA EF1Alpha-puro-T2A-BFP	Gilbert et al., 2014	Addgene #60955
Cyrano conditional knockout targeting vector	This paper	N/A
pcDNA3.1-mCherry	This paper	N/A
pcDNA3.1-mCherry-CyrCR1	This paper	N/A
pcDNA3.1-mCherry-CyrCR1.mutant	This paper	N/A
pcDNA3.1-mCherry-CyrCR1.miR16	This paper	N/A
pcDNA3.1-mCherry-CyrCR1.miR17	This paper	N/A
pU6-sgRNA EF1Alpha-puro-T2A-BFP.Control	This paper	N/A
pU6-sgRNA EF1Alpha-puro-T2A-BFP.CYRANO	This paper	N/A
pU6-sgRNA EF1Alpha-puro-T2A-BFP.PAPD4-1	This paper	N/A
pU6-sgRNA EF1Alpha-puro-T2A-BFP.PAPD4-2	This paper	N/A
pU6-sgRNA EF1Alpha-puro-T2A-BFP.PAPD4-3	This paper	N/A
pU6-sgRNA EF1Alpha-puro-T2A-BFP.PARN-1	This paper	N/A
pU6-sgRNA EF1Alpha-puro-T2A-BFP.PARN-2	This paper	N/A
pU6-sgRNA EF1Alpha-puro-T2A-BFP.PARN-3	This paper	N/A
pU6-sgRNA EF1Alpha-puro-T2A-BFP.DIS3L2-1	This paper	N/A
pU6-sgRNA EF1Alpha-puro-T2A-BFP.DIS3L2-2	This paper	N/A
pU6-sgRNA EF1Alpha-puro-T2A-BFP.DIS3L2-3	This paper	N/A
Software and Algorithms		
STAR RNA-seq Aligner	Dobin et al., 2013	https://github.com/alexdobin/STAR
Htseq-count	Anders et al., 2015	https://htseq.readthedocs.io/en/release_0.9.1/

(Continued on next page)

Continued

REAGENT or RESOURCE	SOURCE	IDENTIFIER
DESeq2	Love et al., 2014	https://bioconductor.org/packages/release/bioc/html/DESeq2.html
Targetscan v7.1	Agarwal et al., 2015	targetscan.org
ImageQuant TL (v8.1.0.0)	GE Healthcare	N/A
GraphPad Prism	GraphPad Software	N/A
ImageJ	NIH	https://imagej.nih.gov/ij/
ImageM (for MATLAB)	Lyubimova et al., 2013	https://github.com/xuebingwu/ImageM
Photoshop CS5.1	Adobe	N/A
Other		
Small-RNA sequencing protocol, step-by-step	Fang and Bartel, 2015	http://bartellab.wi.mit.edu/protocols.html
CRISPRi guide cloning protocol, step-by-step	Gilbert et al., 2014	http://weissmanlab.ucsf.edu/CRISPR/CRISPR.html
Small-RNA blot protocol, step-by-step	Fang and Bartel, 2015	http://bartellab.wi.mit.edu/protocols.html

CONTACT FOR REAGENT AND RESOURCE SHARING

Further information and requests for resources and reagents should be directed to and will be fulfilled by the Lead Contact, David Bartel (dbartel@wi.mit.edu).

EXPERIMENTAL MODEL AND SUBJECT DETAILS**Mouse husbandry**

Mice were group-housed in a 12 hr light/dark cycle (light between 07:00 and 19:00) in a temperature-controlled room ($21.1 \pm 1.1^\circ\text{C}$) at the Whitehead Institute for Biomedical Research with free access to water and food and maintained according to protocols approved by the Massachusetts Institute of Technology Committee on Animal Care. Euthanasia was performed by CO₂ inhalation. The ages of mice are indicated in the figure legends or methods. Sex was not determined for embryos or neonatal pups. For analyses of older animals ($\geq P21$), only male mice were used unless indicated otherwise.

Generation of *Cyrano*^{fl/fl} and *Cyrano*^{-/-} mice

Mice carrying a conditional allele of the *Cyrano* gene (*Cyrano*^{fl/fl} mice) were generated by homologous recombination. The targeting vector was designed to insert a LoxP site in intron 2 and in a poorly conserved region of exon 3. This vector was based on the pPGKneoF2L2DTA vector (a gift from Philippe Soriano, Addgene #13445) and was constructed using genomic sequences amplified by PCR from a BAC clone (RP23-59M9; C57BL/6J; BAC-PAC Resources, Oakland, CA). The LoxP sites were flanked by 4.3 kb 5' and 2.0 kb 3' homology arms. NotI-linearized targeting construct was electroporated into hybrid 129S6;C57BL/6J embryonic stem cells (ESCs). ESC colonies were screened for correct targeting by PCR and Southern blotting, and correctly targeted ESC clones were aggregated with albino CD-1 embryos and transferred into pseudopregnant recipient females. Chimeras were bred with FLPe transgenic mice (Cat #003946, Jackson Laboratories) to excise the neomycin resistance cassette. *Cyrano*^{fl/+} mice were crossed to CMV-Cre transgenic mice (Cat #006054, Jackson Laboratories) to generate *Cyrano*^{+/-} mice and then bred away from the FLPe and Cre transgenes. *Cyrano*^{fl/+} and *Cyrano*^{+/-} mice were each backcrossed ≥ 8 generations into C57BL/6J (Cat #000664, Jackson Laboratories).

Generation of mutant mice using Cas9

Mice with mutations in the miR-7 site of *Cyrano* (*Cyrano*^M mice) were generated by injecting one-cell C57BL/6J embryos with Cas9 RNA and an sgRNA designed to cut within the miR-7 site (Figure 2A; Table S3). F0 mice containing mutations in the miR-7 site were crossed to wild-type C57BL/6J mice to generate heterozygotes and then heterozygotes with the same allele were bred to homozygosity. In total, we generated 6 lines, each with a unique mutant allele, M1–M6 (Figure 2A).

Mir7a1^{-/-}; *Mir7b*^{-/-} mice were generated by injecting one-cell C57BL/6J embryos with Cas9 RNA and three pairs of sgRNAs—each pair of sgRNAs designed to excise the DNA encoding the pre-miRNA hairpin for a different miR-7 locus (Figure S6B; Table S3). Of 102 F0 mice, one had homozygous deletions of both *Mir7a1* and *Mir7b* (Figure S6B), and several had heterozygous deletions of *Mir7a1* and/or *Mir7b*. None had a deleted allele of *Mir7a2*. The double-knockout founder was crossed to C57BL/6J, and then the double-heterozygous F1s were intercrossed to generate *Mir7a1*^{-/-}; *Mir7b*^{-/-} mice.

Mice with mutations in the miR-671 site of *Cdr1as* (*Cdr1as*⁶⁷¹ mice) were generated by injecting one-cell C57BL/6J embryos with Cas9 RNA and an sgRNA designed to cut within the miR-671 site (Figure S6G; Table S3). F0 mice containing deletions (18 and 54 nt, respectively) in the miR-671 site were bred directly to *Cyrano*^{+/-} mice, and then F1 mice were intercrossed to generate lines with the desired homozygous mutations.

Genotyping

Genomic DNA was extracted from mouse earsnips using the HotSHOT method (Truett et al., 2000). For *Cyrano*^M mice, PCR was performed with KAPA HiFi HotStart ReadyMix (Roche), and amplicons were purified (QiaQuick PCR Purification Kit, QIAGEN) and submitted for Sanger sequencing. For all other mutant mice, PCR was performed with KAPA 2G Fast Genotyping Mix (Roche), and amplicons were analyzed by agarose gel electrophoresis. PCR primers, PCR conditions, and expected amplicon sizes are indicated in Table S3.

Cell lines and cell culture

All cells were cultured at 37°C with 5% CO₂. Human cell lines were cultured as follows: HEK293, HEK293T, HeLa, and MCF-7 in DMEM (GIBCO) with 10% FBS (Clontech); SH-SY5Y and SK-N-SH in DMEM/F12 (GIBCO) with 10% FBS; K562 in RPMI-1640 (Life Technologies) with 10% FBS. Mouse cell lines were cultured as follows: C2C12 in DMEM with 10% FBS; Neuro2a in 1:1 DMEM: Opti-MEM (GIBCO) with 10% FBS. Reverse transfections were performed with Lipofectamine 2000 (Life Technologies) according to the manufacturer's protocol. Transfection efficiencies, as estimated by microscopic evaluation of mCherry expression at 24 h, were > 90%. Each of these cell lines is of female origin.

CRISPRi-based knockdown cell lines

Stable CRISPRi cell lines (MCF-7, SH-SY5Y, SK-N-SH, C2C12, HeLa) were generated by transduction with lentivirus carrying constitutively expressed dCas9-KRAB (Gilbert et al., 2013) (Addgene #46911). The CRISPRi K562 cell line expressed a doxycycline-inducible KRAB-dCas9 (Gilbert et al., 2014). Each stable CRISPRi cell line was transduced with lentivirus expressing an sgRNA, which was directed against either the TSS (transcription start site) region of the target gene, the TSS region of *Cyrano*, or no gene (a non-targeting negative-control sgRNA). sgRNA vectors were generated from the pu6-sgRNA EF1Alpha-puro-T2A-BFP plasmid (Addgene #60955) and prepared as described (Gilbert et al., 2014) using oligonucleotides (Table S3). After ~10 days of selection for sgRNA expression with puromycin (1 µg/mL in K562, 2 µg/mL in HeLa, 2.5 µg/mL in SH-SY5Y, and 3 µg/mL in MCF-7, SK-N-SH, and C2C12; Clontech), cells were harvested for RNA extraction. In the case of the inducible K562 cell line, doxycycline (Clontech) was added simultaneously with puromycin and adjusted daily to a concentration of 50 ng/mL, under the assumption of a 24 h half-life in culture (Gilbert et al., 2014).

Primary neuronal cultures

CGN cultures were prepared from male and female P5–P6 neonates as described (Lee et al., 2009) with some modifications. Neonates were decapitated with scissors and the cerebellum and midbrain were pinched off with forceps and transferred to a Petri dish containing ice-cold HBSS-glucose (Hank's Balanced Salt Solution, Life Technologies, 0.6% w/v glucose, 0.035% w/v sodium bicarbonate). Under a dissecting microscope, the cerebellum was detached from the meninges and midbrain and placed in an HBSS-glucose-containing 15 mL conical tube on ice. Additional cerebella were isolated, switching Petri dishes every three neonates, and cerebella from the same genotype were stored together.

Tissue dissociation was performed using the Papain Dissociation System kit (Worthington). Cerebella were incubated in papain solution (Earle's Balanced Salt Solution, 20 U/mL Papain, 100 U/mL DNase) at 37°C for 15–20 min, gently inverting the tube every 4 min. The tissue was triturated 10–12 strokes with an FBS-coated P1000 pipet tip and the supernatant was transferred to a new tube. Cells were pelleted at 200 g for 5 min, supernatant was removed, and cells were resuspended in resuspension solution (Earle's Balanced Salt Solution, 10% albumin-ovomucoid inhibitor solution, ~100 U/mL DNase) using an FBS-coated pipet tip. The cell suspension was gently added to the top of a 15 mL conical tube containing 5 mL of albumin-ovomucoid inhibitor solution and centrifuged at 70 g for 6 min to separate intact cells from cell fragments and membranes. The supernatant was discarded and the pellet resuspended in 3–5 mL of serum-free media (Neurobasal medium, minus phenol red, supplemented with 1x GlutaMAX [Gibco], 100 U/mL penicillin-streptomycin [Gibco], 25 mM KCl, and 1x B-27 [Gibco]) then passed through a 70 µm cell strainer (BD Falcon). Cells were stained with Trypan Blue (Sigma Aldrich) and counted using a Countess cell counter (Thermo Fisher). Each cerebellum yielded 3–6 million cells with > 90% viability.

Cells were plated either at ~50,000 cells/cm² on #1 glass coverslips (Electron Microscopy Sciences) coated with poly-D-lysine (50 µg/mL; EMD Millipore) and laminin (2 µg/mL; Corning) and placed in 12-well plates or at ~90,000 cells/cm² on tissue culture plates coated with poly-D-lysine (50 µg/mL). On DIV1, the media was exchanged for serum-free media containing 10 µM cytosine β-D-arabinofuranoside (AraC; Sigma Aldrich). On DIV3, the media was exchanged for serum-free media. Neurons were fed via half-media exchanges every 2–3 days thereafter. Culture viability was assessed by light microscopy. A subset of cultures were also examined by DAPI staining and immunofluorescence with anti-MAP2 (1:200; EMD Millipore), anti-Tau (1:500; Synaptic Systems), and/or anti-GFAP (1:500; Dako) antibodies to ascertain the fractions of neuronal and glial cells. These cultures typically were ~90% neuronal and consisted predominantly of smaller neurons with 2–5 processes, as expected for CGNs.

Hippocampal cultures were prepared as described (Beaudoin et al., 2012) with slight modifications. Hippocampi were dissected from male and female P0–P1 mouse pups in ice-cold dissection media, washed twice with ice-cold dissection media, trypsinized for 20 min at 37°C, and then treated with 0.1% DNase for 2 min at room temperature. Tissue was washed again in room-temperature dissection media and brought up to 10 mL in plating media. The tissue was then triturated in a 15 mL conical tube with an FBS-coated 5 mL serological pipet in 3 batches, performing no more than 10 triturations per batch and transferring the dissociated cells to a new 15 mL conical tube between each batch. Dissociated cells were passed through a 70 µm cell strainer, counted, and plated in plating media at ~100,000 cells/cm² on tissue culture plates coated with poly-D-lysine (50 µg/mL). Plating media was exchanged for maintenance media between 2–6 h after plating. On DIV2, cells were treated with 5 µM AraC for 24 h and then maintenance media was fully exchanged. Neurons were fed via half-media exchanges every 3 days thereafter.

METHOD DETAILS

RNA extraction

For cells, total RNA was extracted with TRI Reagent (Life Technologies) according to the manufacturer's protocol. For adherent cells, TRI Reagent was added directly to the tissue culture plate, and cells were quickly detached by scraping. For suspension cells, cells were first pelleted by centrifugation. For mouse tissue, total RNA was extracted with TRI Reagent according to the manufacturer's protocol with the following modifications. Mouse tissues were rapidly dissected after euthanasia (CO₂) and flash frozen in Eppendorf tubes in liquid N₂. Tissue was transferred to a 15 mL conical tube, 1–2 mL of TRI Reagent was added, and the tissue was homogenized with a TissueRuptor (QIAGEN) and disposable probes. Samples were aliquoted in Eppendorf tubes (1 mL per tube) and phase separation was achieved with either 200 µL chloroform (J.T. Baker Analytical) or 100 µL 1-Bromo-3-chloropropane (Sigma). For samples with high fat content, such as brain tissue, 2–3 volumes of 1-Bromo-3-chloropropane were necessary to fully separate the aqueous and organic layers. After isopropanol precipitation and two 70% ethanol washes, all RNA was resuspended in water.

Cytoplasmic/nuclear fractionation

Cytoplasmic and nuclear fractions of each cell line were isolated via mild lysis and centrifugation as follows. No more than 10⁷ cells were harvested and pelleted by centrifuging at 300 g for 5 min. The plasma membrane was lysed by adding 175 µL of precooled RLN+EDTA buffer (50 mM Tris, pH 8.0, 140 mM NaCl, 1.5 mM MgCl₂, 0.5% NP-40, 10 mM EDTA) freshly spiked with 1 µL/mL Superasin and 1 mM DTT and gently resuspended by pipetting, avoiding vigorous handling as this can cause partial nuclear lysis. Lysates were incubated on ice for 5 min then centrifuged at 500 g for 5 min to pellet nuclei. The supernatant was transferred to a new tube and spun again at 500 g for 1 min to remove any contaminating nuclei. The supernatant was transferred to a new tube containing 1 mL of TRI Reagent and vortexed vigorously. Meanwhile, the original nuclear pellet was washed once with 175 µL of precooled RLN+EDTA and spun at 500 g for 1 min. After aspirating the supernatant, the nuclei were gently resuspended in 175 µL of precooled RLN+EDTA. 1 µL was saved for microscopic confirmation of intact nuclei, and the remainder was added to a new tube containing 1 mL of TRI Reagent, vortexed vigorously, and passed through a 20-gauge needle at least 5 times. 25 pg of uncapped firefly luciferase RNA containing a 30-base poly(A) tail (Promega #L4561) was added to each fraction in TRI Reagent prior to RNA extraction.

Lentivirus production and transduction

HEK293T cells were used to package lentivirus. In a 6-well tissue culture plate, ~170,000 cells/cm² were reverse-transfected with 1.4 µg transfer plasmid, 0.94 µg pCMV-dR8.91 packaging plasmid (a gift from Jonathan Weissman), and 0.47 µg pMD2.G envelope plasmid (a gift from Didier Trono; Addgene #12259) using Lipofectamine 2000 (Thermo Fisher). After 72 h, the media was collected and centrifuged at 500 g for 10 min to pellet debris. To infect cells, 250 µL of virus-containing supernatant (~1/7th of the total) was combined with 750 µL media and 8 µg/mL polybrene (Santa Cruz Biotechnology) and then added to one well of a 12-well plate (containing either 200,000 suspension cells or adherent cells plated 24 h before at 25,000/cm²). Plates were centrifuged at 12,000 g for 90 min at room temperature then returned to the 37°C incubator.

RNA-seq

Each poly(A)-selected RNA-seq library was prepared from 4 µg total RNA. For profiling predicted miR-7 targets in *Cyrano*^{-/-} mice (Figure 4), libraries were prepared using the unstranded TruSeq kit (Illumina) with RNA from tissues from 4-month-old male wild-type and *Cyrano*^{-/-} littermates on a mixed 129S6; C57BL/6J background (1 replicate per library; n = 4–6 libraries per genotype for each tissue). For profiling mRNAs and noncoding RNAs (Figures 1A, 5A, 6A, S5A, S5B, and S6E), libraries were prepared using the stranded NEXTflex kit (Bioo Scientific) with RNA from cerebella from 1-month-old male wild-type, *Cyrano*^{-/-}, *Cyrano*^{M3/M3} and *Mir7a1*^{-/-}; *Mir7b*^{-/-} mice on a C57BL/6J background (1 replicate per library; n = 3–4 libraries per genotype). All libraries were sequenced on the Illumina HiSeq platform with 40 nt single-end reads.

Reads were aligned to the mouse genome (mm10) using STAR v2.4 (Dobin et al., 2013) with the parameters “–outFilterType BySJout–outFilterIntronMotifs RemoveNoncanonicalUnannotated–outSAMtype BAM SortedByCoordinate.” Aligned reads were assigned to genes using annotations from Ensembl (*Mus_musculus*.GRCm38.73.gtf; downloaded October 15, 2014) and htseq-count v0.6.1p1 (Anders et al., 2015) with the parameters “-m union -s no” for unstranded libraries and “-m union -s reverse” for stranded libraries. An annotation for Cdr1as (chrX: 61183248–61186174) was manually added to the gtf file. For counting pri-miR-7 species,

Mir7 annotations were extended 200 nt on both the 5' and 3' ends, and the pre-miR-7 sequences were excluded from the annotation. Count files were merged to generate tables of counts for each tissue organized by genotype. Differential expression was determined using DESeq2 v1.10–v1.18 (Love et al., 2014) with the parameter “betaPrior = FALSE” and without the IfcShrink function. For RNA-seq plots (Figures 5D and 6A), only RNAs with a mean RPM > 1 in wild-type samples and a CV < 10 standard deviations above the median CV in both wild-type and mutant samples are shown. RNA-seq browser tracks were visualized in the UCSC genome browser and IGV v2.3.34 (Thorvaldsdóttir et al., 2013).

The effects of miR-7 on target mRNA levels were determined by comparing fold changes for mRNAs containing miR-7 sites in their 3' UTRs relative to those observed for control mRNAs. All predicted miR-7 targets were downloaded from TargetScanMouse v7.1 (Agarwal et al., 2015) and grouped by conservation of miR-7 targeting and by cumulative weighted context++ score to generate a set of conserved predicted targets and a set of top predicted targets, respectively. The set of no-site controls consisted of mRNAs lacking a perfect 6-nt seed match to miR-7 anywhere within the mature mRNA. For each tissue, only mRNAs with > 50 mean counts (approximately equivalent to 5 RPM), as determined by DESeq2, were analyzed. Predicted targets generally have longer 3' UTRs than no-site mRNAs; to minimize fold-change effects that correlate with 3'-UTR-length differences (rather than the presence of a miR-7 site), we normalized all fold changes based on mRNA 3' UTR lengths (as annotated in Eichhorn et al., 2014). To do this, we first fit a linear function to the relationship between fold change and 3'-UTR length for no-site mRNAs and then used this function to normalize the fold changes for all mRNAs.

Small-RNA sequencing

Library preparation started with 5 µg of total RNA from either tissues of 1-month-old male mice on a C57BL/6J background or stable CRISPRi K562 cell lines. From each total RNA sample, RNAs that co-migrated within the range of 18 and 32 nt radiolabeled internal standards were isolated on a 15% polyacrylamide urea gel. Purified RNA was ligated to a preadenylated 3' adaptor using T4 RNA Ligase 2 KQ mutant (NEB) in a reaction supplemented with 10% polyethylene glycol (PEG 8000, NEB). To reduce ligation biases, this 3' adaptor had four random-sequence positions at its 5' end. After gel purification on a 10% polyacrylamide urea gel, RNA was ligated to a 5' adaptor using T4 RNA Ligase I (NEB) in a reaction supplemented with 10% PEG. To reduce ligation biases, this adaptor had eight random-sequence positions at its 3' end. After gel purification on a 8% polyacrylamide urea gel, RNA was reverse transcribed with SuperScript III (Invitrogen), and the cDNA was amplified 8–12 cycles with KAPA HiFi DNA polymerase (Kapa Biosystems). Amplified DNA was purified on an 8% polyacrylamide 90% formamide gel and submitted for sequencing. A step-by-step protocol for constructing libraries for small-RNA sequencing is available at <http://bartellab.wi.mit.edu/protocols.html>. Libraries were sequenced on the Illumina HiSeq platform with 50 nt single-end reads. Reads were trimmed of adaptor sequence using cutadapt (Martin, 2011) and filtered using fastq_quality_filter (FastX Toolkit; http://hannonlab.cshl.edu/fastx_toolkit/) with the parameters “-q 30 –p 100” to ensure that all bases had an accuracy of 99.9%.

To count the miRNAs in each library, the first 18 nt of each read were string-matched to a dictionary of miRNA sequences. Mouse and human miRNA dictionaries were based on annotations in miRbase_v20 and miRbase_v21, respectively. Matching to the first 18 nt had the advantage of combining all miRNA isoforms into a single count but also can result in ambiguous read assignments for mature miRNAs from distinct loci that are identical for the first 18 nt but differ at one or more positions closer to their 3' ends (such as let-7a-5p and let-7c-5p). To avoid this ambiguity, these miRNAs (< 5% of all annotations) were removed from the dictionary. Count files were merged to generate tables of counts for each tissue organized by genotype. Differential expression was determined using DESeq2 (Love et al., 2014) with the parameter “betaPrior = FALSE.” For small-RNA sequencing plots (Figures 2A, 2B, 2D, S6G, and S6H), only miRNAs with a mean RPM > 1 in wild-type samples and a CV < 5 standard deviations above the median CV in both wild-type and mutant samples are shown.

For analyses of tailing and trimming, we used the same string-matching described above while also binning reads by lengths from 19–30 nt. For each miRNA with a mean RPM > 100, we calculated the fraction of reads of each length. Any length with a fraction > 14.5% was considered “mature” (this percentage was selected to include both the 23 and 24 nt isoforms of miR-7 in all samples). Trimmed reads were all reads shorter than the shortest mature length, and tailed reads were all reads longer than the longest mature length. In this fashion, we were able to determine the aggregate number of trimmed and tailed reads for each miRNA. To identify the nucleotide(s) added during tailing, we used custom scripts to count all homopolymers appended to mature miR-7 (both the 23 and 24 nt isoforms).

Northern blots

For each sample, 1–10 µg of total RNA was resolved on a denaturing polyacrylamide gel, transferred onto a Hybond-NX membrane (GE Healthcare) using a semi-dry transfer apparatus (Bio-Rad), and incubated at 60°C for 1 h with EDC (N-(3-dimethylaminopropyl)-N'-ethylcarbodiimide; Thermo Scientific) diluted in 1-methylimidazole to chemically crosslink 5' phosphates to the membrane. Blots were hybridized to radiolabeled DNA or LNA oligonucleotide probes (Table S3). Northern-blot results were analyzed with ImageQuant TL (v8.1.0.0). A step-by-step protocol is available at <http://bartellab.wi.mit.edu/protocols.html>. For some experiments, synthetic miR-7 standards were run in lanes adjacent to the experimental samples to generate a standard curve used for absolute quantification.

RT-qPCR

For mouse tissues, 1 µg total RNA was treated with RQ1 DNase (Promega) or Turbo DNase (Life Technologies), then reverse transcribed with Superscript III (Life Technologies) and either oligo(dT) primers (cytoplasm/nuclear fractionation experiments) or random hexamers (all other experiments). Expression of Cyrano and Cdr1as were measured by qPCR (primers listed in [Table S3](#)) using SYBR Green (Applied Biosystems) on a QuantStudio 6 system (Applied Biosystems) and quantified using the $\Delta\Delta CT$ method with either *Actb* expression or the geometric mean of *Actb*, U1, U2, and U6 expression as the internal normalization control.

For stable CRISPRi cell lines, 1 µg total RNA was reverse transcribed with QuantiTect RT Kit (QIAGEN) followed by qPCR using SYBR Green. Expression of CYRANO and mRNAs were quantified (primers listed in [Table S3](#)) using the $\Delta\Delta CT$ method with the geometric mean of *GAPDH*, *ACTN1*, U1, U2, and U6 expression as the internal normalization control and the non-targeted sample as the inter-sample normalization control.

Absolute quantification of miR-7, Cyrano, and Cdr1as in CGNs and cell lines

To quantify the number of molecules of a given RNA per cell, we first determined the amount of total RNA per cell. For this, total RNA was extracted and quantified from a defined number of cells, with the assumption of negligible RNA loss. For human cell lines, cell number was determined using a Countess cell counter. For mouse DIV11 CGNs, cell number was determined from light micrographs of 6-well plates (10 20x images per sample) prior to RNA extraction. By this method, we estimated mean total RNA per cell as 7.7 pg per CGN, 19.9 pg per HEK293T cell, and 23.2 pg per HeLa cell ($n = 3$ samples per cell type; [Table S2](#)).

Next, we generated standards for miR-7, Cyrano, and Cdr1as. For miR-7, 10 pmol of a 23-mer RNA oligo (IDT) matching the human miR-7 and mouse miR-7a sequence was PNK-labeled with cold ATP, desalting on a P30 column (Bio-Rad) and then serially diluted in 200 ng/µL yeast tRNA (Life Technologies). For Cyrano, the first 3.5 kb of the mouse Cyrano cDNA and the first 3.7 kb of the human CYRANO cDNA were PCR amplified, using primers that added a T7-promotor sequence. After purification on an agarose gel (Qiaquick Gel Extraction, QIAGEN), 1 pmol of each PCR product was *in vitro* transcribed with T7 MEGAscript (Ambion), according to manufacturer's protocol, and cleaned up with Turbo DNase and MEGAclean (Ambion). Full-length RNA was mixed with deionized formamide (final concentration 60% v/v) and 6x loading dye, heated to 65°C for 5 min, snap-cooled on ice, and then size-selected on a native RNase-free 1% agarose gel run at 70V with RiboRuler HR ladder (Thermo Scientific). Size-selected RNA was purified with Zymoclean Gel RNA Recovery Kit (Zymo Research), and quantified on a NanoDrop spectrophotometer (Thermo Scientific). For Cdr1as, a 243 bp fragment of mouse Cdr1as and a 362 bp fragment of human CDR1AS, each containing the back-splice junction and each prepended with the T7-promotor sequence, were ordered from IDT as gBlocks ([Table S3](#)). Approximately 1 pmol of dsDNA was *in vitro* transcribed with T7 MEGAshortscript (Ambion) according to manufacturer's protocol and then cleaned up with MEGAclean. The full-length RNAs were purified on a 4% polyacrylamide gel run with RNA Century markers (Ambion), eluted overnight at 4°C, purified with a Spin-X column (Corning), concentrated by EtOH precipitation, and quantified by NanoDrop. The molecular weight of each RNA standard was calculated based on its sequence (1,503,509.3 g/mol for mouse Cyrano; 1,147,517.4 g/mol for human Cyrano; 70,377.1 g/mol for mouse Cdr1as; 108,587.7 g/mol for human Cdr1as) and RNA standards were serially diluted, 10^{10} to 10^4 copies, in 0.2 µg/µL total RNA derived from either HeLa cells (for mouse standards) or 3T3 cells (for human standards).

To determine absolute amounts of miR-7, 5 µg total RNA from CGN and HEK293T and 15 µg total RNA from HeLa were analyzed by northern blot alongside a serial dilution of synthetic miR-7 standards. To determine absolute amounts of Cyrano and Cdr1as, RT-qPCR with Superscript III and gene-specific primers ([Table S3](#)) was performed on 1 µg total RNA from CGN, HEK293T, and HeLa alongside 5 µL of each serial dilution of *in vitro* transcribed standard. For each RNA of interest, knowing the absolute amount of this RNA per µg of total RNA as well as the amount of total RNA per cell enabled calculation of the number of molecules of this RNA per cell.

Single-molecule FISH

Single-molecule FISH ([Batish et al., 2011](#)) was performed on CGNs grown on glass coverslips according to the following protocol. Cells were washed twice in PBS (Ambion) and fixed for 10 min in freshly prepared 4% paraformaldehyde (Electron Microscopy Sciences) in PBS. After aspirating the fixation solution, cells were gently washed in PBS and then stored in 70% ethanol for ≥ 2 h (up to 2 weeks) at 4°C. Before probing, coverslips were equilibrated for ≥ 2 min in washing buffer (10% formamide, 2X SSC). Custom probes 3' end-modified with Quasar 670 dye ([Table S3](#)) were diluted to 25 nM in hybridization solution (10% formamide, 2X SSC, 100 mg/mL dextran sulfate), and 50 µL of probe/hybridization mix was dotted on parafilm pressed to a glass plate, 1 dot per coverslip. Coverslips were removed from washing buffer with forceps and then placed on the probe/hybridization mix with the cell side facing the liquid. From this point forward, coverslips were protected from light as much as possible to minimize photobleaching of the 670 dye. After incubating overnight in a humidifying chamber at 37°C, the coverslips were washed 30 min in washing buffer to remove excess probe, 30 min in washing buffer containing 100 ng/mL DAPI, and 5 min in washing buffer to remove excess DAPI. Coverslips were mounted on glass slides with ProLong Gold (Invitrogen) and allowed to cure overnight before sealing with clear nail polish.

Images were acquired using a 100x oil-immersion objective with a numerical aperture of 1.4 on a wide-field fluorescence microscope (either a Zeiss AxioPlan2 with cooled CCD camera or a GE Healthcare Deltavision with sCMOS camera). In each field, 10–30 z sections with 0.2 µm spacing were acquired. On the AxioPlan2, exposure times were 2 s Cy5, 0.5 s GFP, 0.5 s DAPI. On the Delta-vision, exposure times were 0.5 s Cy5 (100% intensity), 0.3 s GFP (100%), 0.01 s DAPI (50%).

For quantification, hot pixels were removed from individual stacks using Remove Outliers (radius 1 pixel, threshold 10) and Despeckle functions in ImageJ. Paired Cy5 and GFP stacks were loaded into the MATLAB program ImageM (Lyubimova et al., 2013), z-projected, and the number of dots in each z-projection was enumerated using the Count Dots feature. After subtracting background dots, defined as those counted in both the Cy5 and GFP stacks, the number of dots was divided by the number of intact, non-pyknotic nuclei in each image to generate the average molecules per cell for each field. In total, 40 fields were analyzed for each probe and each genotype. To quantify the number of dots by subcellular location, the Segmentation feature in ImageM was used to outline either the soma using GFP autofluorescence or the nucleus using DAPI. In this fashion, the number of dots in the nucleus was determined directly, the number of dots in the cytoplasmic soma was calculated by subtracting nuclear dots from soma dots, and the number of dots in neuronal processes was calculated by subtracting soma dots from total dots per field. We note that because quantification was performed on z-projected images rather than individual sections in a z stack, any dots above or below the nucleus would have been assigned to the nucleus. For generating images for figures, hot pixels were removed as described above, stacks were z-projected using the Max Intensity function and then combined using the Merge function in ImageJ. Merged files were converted to an RGB file and imported into Photoshop (Adobe) for cropping.

QUANTIFICATION AND STATISTICAL ANALYSIS

Graphs were generated in GraphPad Prism 7 and statistical analyses were performed using Excel or Graphpad Prism 7. Statistical parameters including the value of n, statistical test, and statistical significance (p value) are reported in the figures and their legends. For studies involving mouse tissues, replicates refer to samples derived from different mice. For studies involving cell culture, replicates refer to either transfections performed on different days or transductions performed on the same day with different viral supernatants derived from transfections performed in parallel. No statistical methods were used to predetermine sample size. Statistical tests were selected based on the desired comparison. Unpaired two-tailed t tests (Excel) were used to assess significance when comparing expression of 1–2 genes (northern-blot analyses, RT-qPCR) between two genotypes. One-way ANOVA (Graphpad) was used to assess significance when comparing expression of 1–2 genes (northern-blot analyses, RT-qPCR) between ≥ 3 genotypes; significant ANOVA results were followed by post hoc testing either comparing every mean with every other mean (Tukey's multiple-comparison test) or comparing every mean to the wild-type mean (Dunnett's multiple-comparison test). For differential expression of global measurements (RNA-seq, small-RNA sequencing), the DESeq2 software generated adjusted p values using the Wald test with the Benjamini-Hochberg procedure to correct for multiple-hypothesis testing. The Mann-Whitney test was used to compare cumulative distributions of mRNA fold changes between two gene sets.

DATA AND SOFTWARE AVAILABILITY

The accession number for the sequencing data reported in this paper is GEO: GSE112635.

Supplemental Figures

Cell

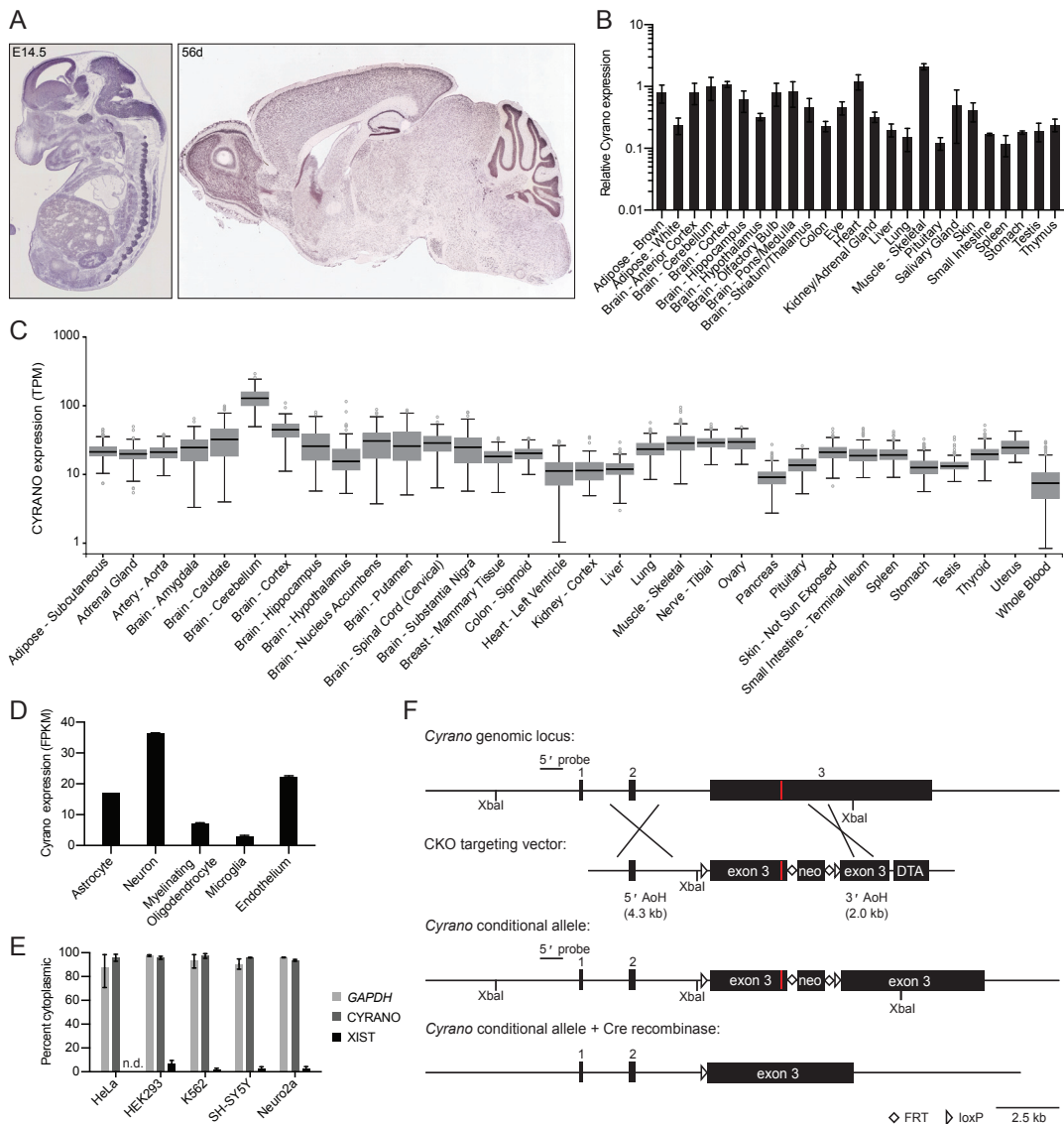


Figure S1. Cyrano Expression, Related to Figure 1

- (A) Images of *in situ* hybridizations for Cyrano in mouse embryo (E14.5) and adult mouse brain (P56) obtained from GenePaint.org (Visel et al., 2004) and the Allen Brain Atlas (Lein et al., 2007), respectively. In both databases, *Cyrano* is annotated as the RIKEN cDNA 1700020l14Rik gene.
- (B) Relative Cyrano expression in 25 tissues of 2-month-old C57BL/6J mice. Shown are mean Cyrano levels, as determined by RT-qPCR, normalized to the geometric mean of the values for four housekeeping genes and relative to cerebellum (error bars, s.d.; n = 3 for each tissue).
- (C) CYRANO expression from RNA-seq of 32 post-mortem human tissues, provided by the GTEx Portal (01/15/2018). Expression values in TPM (transcripts per million) are shown as boxplots (box, 25th, median, and 75th percentiles; whiskers, 1.5 times the interquartile range). In the GTEx Portal, CYRANO is annotated as the *OIP5-AS1* gene.
- (D) Cyrano expression from RNA-seq of purified cell populations from the mouse cortex (Dong et al., 2015). Mean expression values in FPKM (fragments per kb per million reads) are shown (error bars, range; n = 2 for each cell type).
- (E) Percentage of CYRANO detected in the cytoplasm of mammalian cell lines. Ratios were determined by RT-qPCR, using RNA from cytoplasmic and nuclear fractions, normalizing to a luciferase spike-in transcript (error bars, range; n = 2 for HEK293, HeLa, and SH-SY5Y, n = 3 for K562 and Neuro2a). For comparison, results for GAPDH mRNA and the nuclear-localized XIST lncRNA are also shown (n.d., not detected above background in cytoplasm).
- (F) Cyrano gene targeting strategy. Shown between the wild-type locus and the recombinant alleles is the vector used to target the first half of exon 3 (black boxes, exons; red line, miR-7 site with extensive pairing; open triangles, loxP sites; open diamonds, FRT sites; neo, neomycin-resistance cassette; DTA, diphtheria toxin A; AoH, arm of homology). Screening of ES cell clones was performed by long-range PCR as well as Southern blot of XbaI-digested genomic DNA with a 5' probe upstream of exon 1.

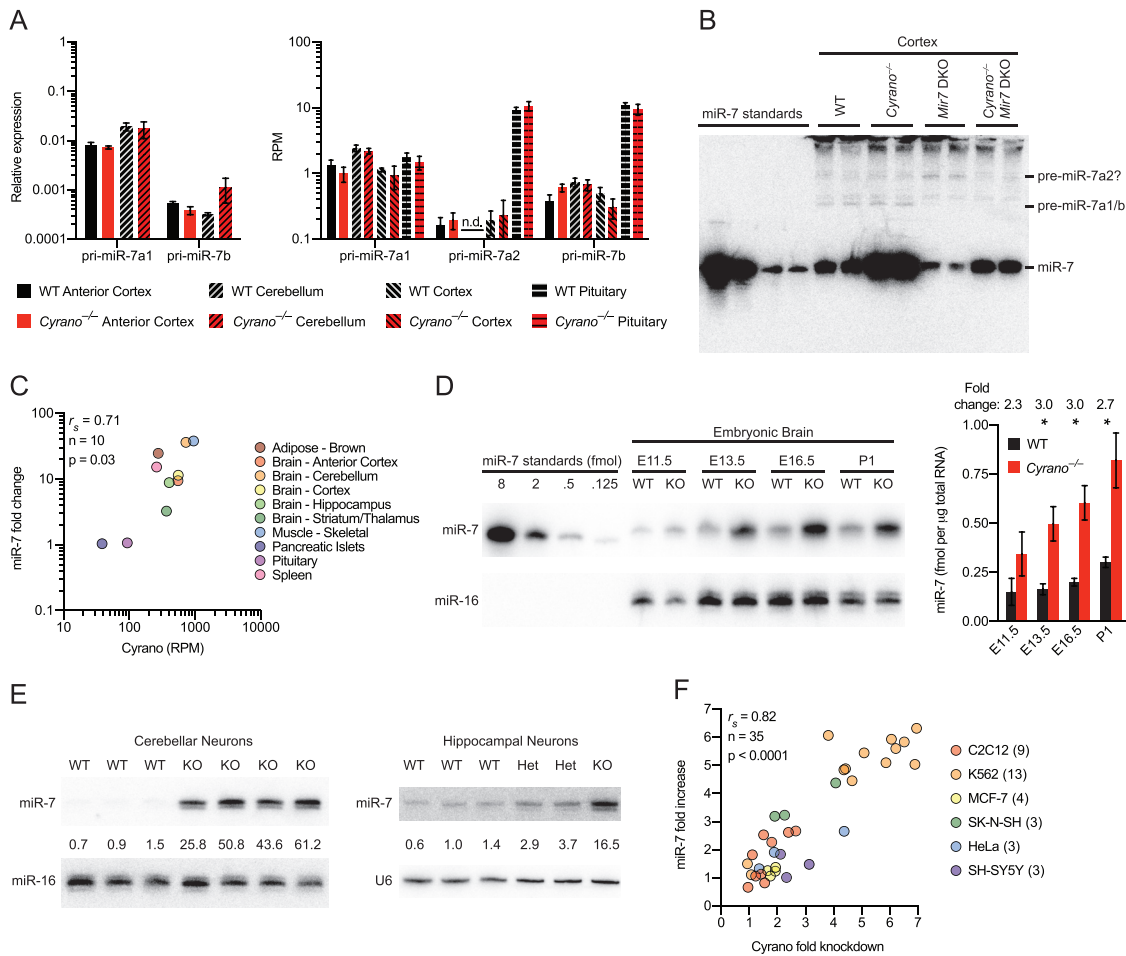


Figure S2. Cyrano Promotes miR-7 Destruction, Related to Figure 1

(A) Influence of Cyrano on pri-miR-7 expression in the brain. The plot on the left shows mean pri-miR-7a1 and pri-miR-7b levels in wild-type (black) and *Cyrano*^{-/-} (red) anterior cortex and cerebellum (key), as determined by RT-qPCR, normalized to the geometric mean of the values for four housekeeping genes (error bars, s.d.; n = 3 per genotype for each tissue). The plot on the right shows mean expression values in RPM (reads per million) for all three pri-miR-7 transcripts in wild-type and *Cyrano*^{-/-} anterior cortex, cerebellum, cortex, and pituitary, as determined by RNA-seq (error bars, s.d.; n = 4–5 per genotype for each tissue; n.d., not detected).

(B) Influence of Cyrano on pre-miR-7 expression. Shown is a representative northern blot measuring miR-7 levels in wild-type and mutant cortex. This blot is an uncropped version of the blot shown in Figure 6C, with the signal increased in order to detect the less-abundant pre-miR-7 species. Levels of pre-miR-7 species (identified by their absence in the *Mir7* DKO) were unchanged in *Cyrano*^{-/-} cortex.

(C) Relationship between miR-7 changes observed after disrupting Cyrano and the level of wild-type Cyrano expression. Shown are miR-7 fold changes from Figure 2C plotted as a function of Cyrano expression in wild-type tissues, as determined from RNA-seq data also used for the analyses of Figure 5C.

(D) Influence of Cyrano on miR-7 expression in developing mouse brain. Shown at the left is a representative northern blot measuring miR-7 levels in wild-type (WT) and *Cyrano*^{-/-} (KO) brain at the indicated developmental time points. Plotted on the right are miR-7 levels in wild-type (black) and *Cyrano*^{-/-} (red) embryonic brain normalized to miR-16 (error bars, s.d.; n = 3 per genotype). Statistically significant fold changes are indicated (*p < 0.05, unpaired two-tailed t test).

(E) Influence of Cyrano on miR-7 expression in cultured primary neurons. Shown are northern blots for wild-type and *Cyrano*^{-/-} DIV11 cerebellar neurons (left) and DIV12 hippocampal neurons (right). Levels of miR-7 (upper panels) were normalized to those of either miR-16 (lower panel, left) or U6 (lower panel, right), and reported relative to the mean wild-type level.

(F) Relationship between the magnitude of miR-7 fold change and extent of CYRANO knockdown. Shown are miR-7 fold changes, measured by northern blot, plotted as a function of CYRANO knockdown, as determined by RT-qPCR, for 35 mammalian CRISPRi cell lines stably expressing dCas9-KRAB and an sgRNA targeting CYRANO. Parental cell lines are indicated (key). For each cell line receiving a targeting sgRNA, levels of CYRANO and miR-7 were normalized to the geometric mean of the values for five housekeeping genes and miR-16, respectively, and shown relative to the non-targeting control.

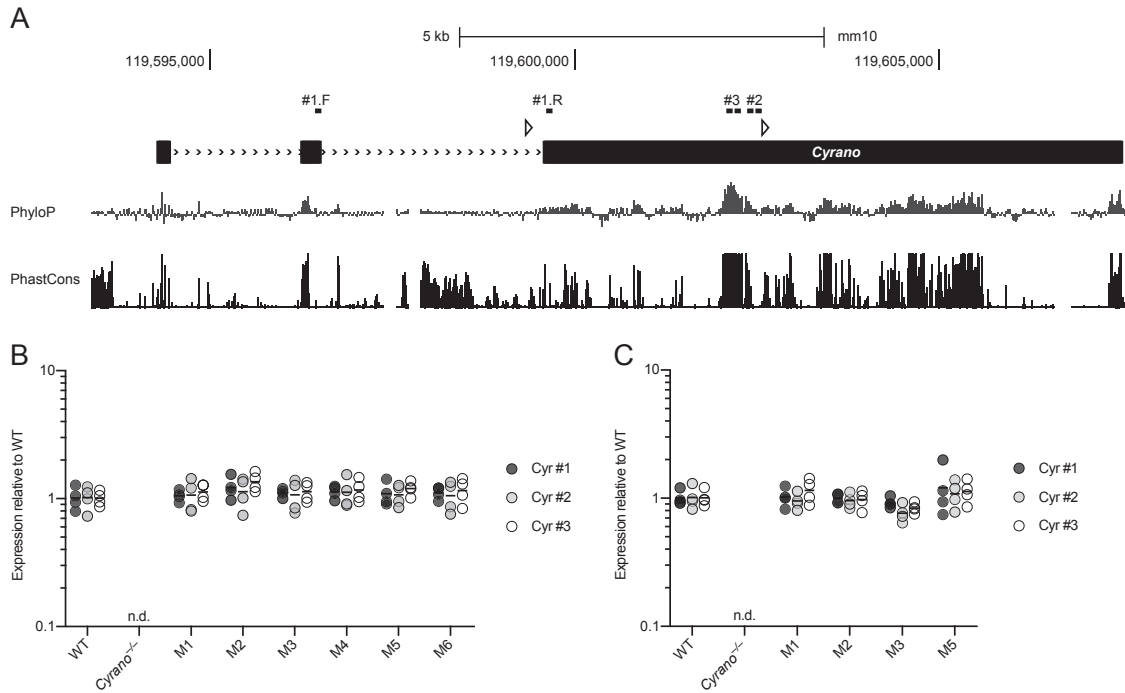


Figure S3. Mutating the miR-7 Site in Cyrano Does Not Cause Detectable Changes in Cyrano Levels, Related to Figure 2

(A) Cyrano locus annotated with binding sites of 3 RT-qPCR primer pairs (#1, #2, #3). Otherwise, this panel is as in Figure 1A.

(B) Cyrano expression in wild-type and mutant cerebellum. Plotted are relative Cyrano levels in wild-type and Cyrano mutant cerebellum, as determined by RT-qPCR with three primer sets pairing to sites mapped in (A). Cyrano levels, normalized to that of *Actb*, are shown as fold changes relative to the mean wild-type expression ($n = 4$ per genotype; n.d., not detected). No significant differences in Cyrano expression were detected (ANOVA with Dunnett's test), indicating that either miR-7 does not influence Cyrano accumulation in this tissue, or abrogated repression at this site is offset by enhanced repression (due to increased levels of miR-7) at a second, more conventional site located at the beginning of exon 3.

(C) Cyrano expression in wild-type and Cyrano mutant pituitary. Otherwise, this panel is as in (B).

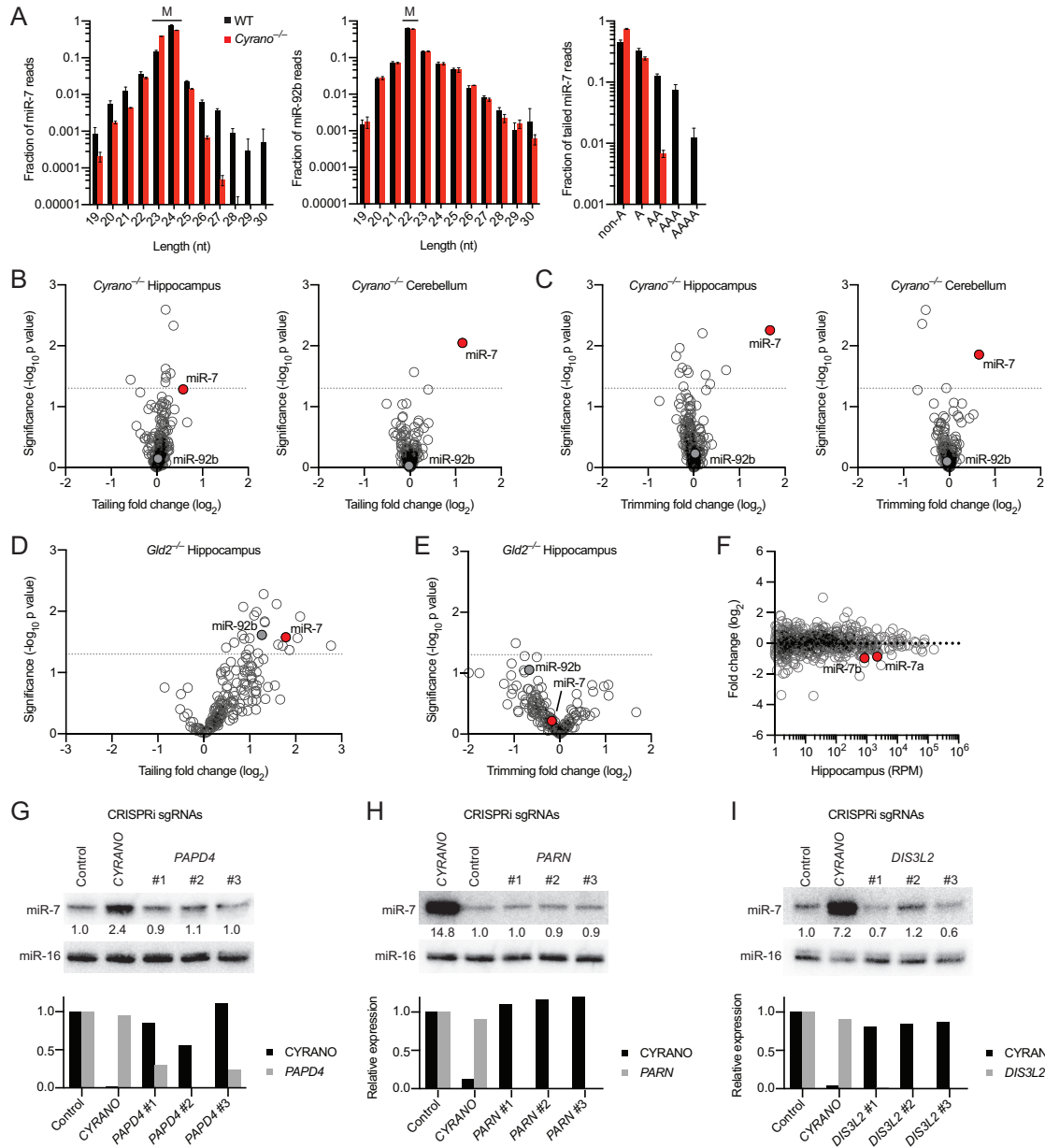


Figure S4. Cyrano Induces Tailing and Trimming of miR-7, but Tailing Appears Dispensable, Related to Figure 3

(A) Influence of Cyrano on miR-7 tailing and trimming in cerebellum. Otherwise, this panel is as in Figure 3A. In both hippocampus and cerebellum, the trimmed miR-7 isoforms largely matched the genome-encoded miR-7 sequence, implying that tailing of trimmed species was either rare or destabilizing.

(B) Influence of Cyrano on global miRNA tailing in hippocampus (left) and cerebellum (right). Shown are aggregate tailing log₂-fold changes for each expressed miRNA after disrupting Cyrano, plotting statistical significance of the change (based on p values determined by unpaired two-tailed t tests, one per miRNA) as a function of the change in WT divided by *Cyrano*^{-/-}. Each circle represents one miRNA, showing results for all miRNAs expressed above 100 RPM (read per million miRNA reads) in wild-type tissue. Circles representing miR-7 (miR-7a and miR-7b were combined for this analysis) and miR-92b are colored red and gray, respectively. Cyrano increased the aggregate tailed fractions 1.5- and 2.2-fold, respectively. Dotted lines indicate a p value of 0.05.

(C) Influence of Cyrano on global miRNA trimming in hippocampus (left) and cerebellum (right). Cyrano increased the aggregate trimmed fractions 3.2- and 1.6-fold, respectively. Otherwise, this panel is as in (B).

(D and E) Influence of Gld2 on global miRNA tailing (D) and trimming (E) in hippocampus, evaluated using data from Mansur et al. (2016). Otherwise, this panel is as in (B and C).

(F) Influence of Gld2 on miRNA levels in hippocampus. Shown are log₂-fold changes in mean miRNA levels observed between wild-type and *Gld2*^{-/-} hippocampus, as determined by small-RNA sequencing (Mansur et al., 2016) and plotted as a function of expression in wild-type hippocampus (n = 6 per genotype). Each circle represents one miRNA, showing results for all miRNAs expressed above 1 RPM (read per million miRNA reads) in wild-type hippocampus. Circles representing miR-7 paralogs are colored red.

(legend continued on next page)

(G) Influence of PAPD4 on miR-7 expression in stable *PAPD4*-knockdown K562 cells. Shown at the top is a northern blot monitoring miR-7 levels in stable cell lines expressing either a control sgRNA or an sgRNA targeting either *CYRANO* or *PAPD4* for CRISPRi-mediated knockdown. The levels of miR-7 are reported relative to the miR-7 level in the control cell line after normalizing to the level of miR-16. Plotted at the bottom are *CYRANO* and *PAPD4* levels, as determined by RT-qPCR, in stable lines cells expressing the indicated sgRNAs. *CYRANO* and *PAPD4* levels were normalized to the geometric mean of the values for five housekeeping genes and plotted relative to levels in the control cell line. The level of *PAPD4* in line #2 was < 2% of that in the control.

(H) Influence of PARN on miR-7 expression. The levels of *PARN* in lines #1–3 were each < 1% of that in the control. Otherwise, this panel is as in (G). One way to reconcile the prevailing idea that tailing is required for TDMD with our observation that miR-7 levels remained unchanged after loss of Gld2 would be to propose that Gld2 has opposing consequences that somehow offset each other. Indeed, for miR-122, monoadenylation by Gld2 stabilizes the miRNA, whereas oligoadenylation by Gld2 destabilizes it by making it a substrate for PARN-catalyzed exonucleolytic decay (Katoh et al., 2015; Katoh et al., 2009). Because monoadenylation of miR-122 predominates, *Gld2* deletion in mice leads to an overall decrease in miR-122 in liver (Katoh et al., 2009). Nevertheless, knockdown of PARN results in increased miR-122, revealing the destabilizing role for oligoadenylation in this context (Katoh et al., 2015). However, the results of this panel, which show that stable knockdown of *PARN* by 99% had no effect on miR-7 levels, suggest that a similar phenomenon is not occurring for miR-7.

(I) Influence of DIS3L2 on miR-7 expression. The levels of *DIS3L2* in lines #2–3 were < 1% of that in the control. Otherwise, this panel is as in (G). Although *DIS3L2* is thought to prefer oligouridylated substrates, a recent biochemical effort to identify factors involved in viral TDMD enriched for Dis3l2 (Haas et al., 2016). However, the results of this panel indicate that CRISPRi knockdown of *DIS3L2* by 98% had no discernable effect on miR-7 levels.

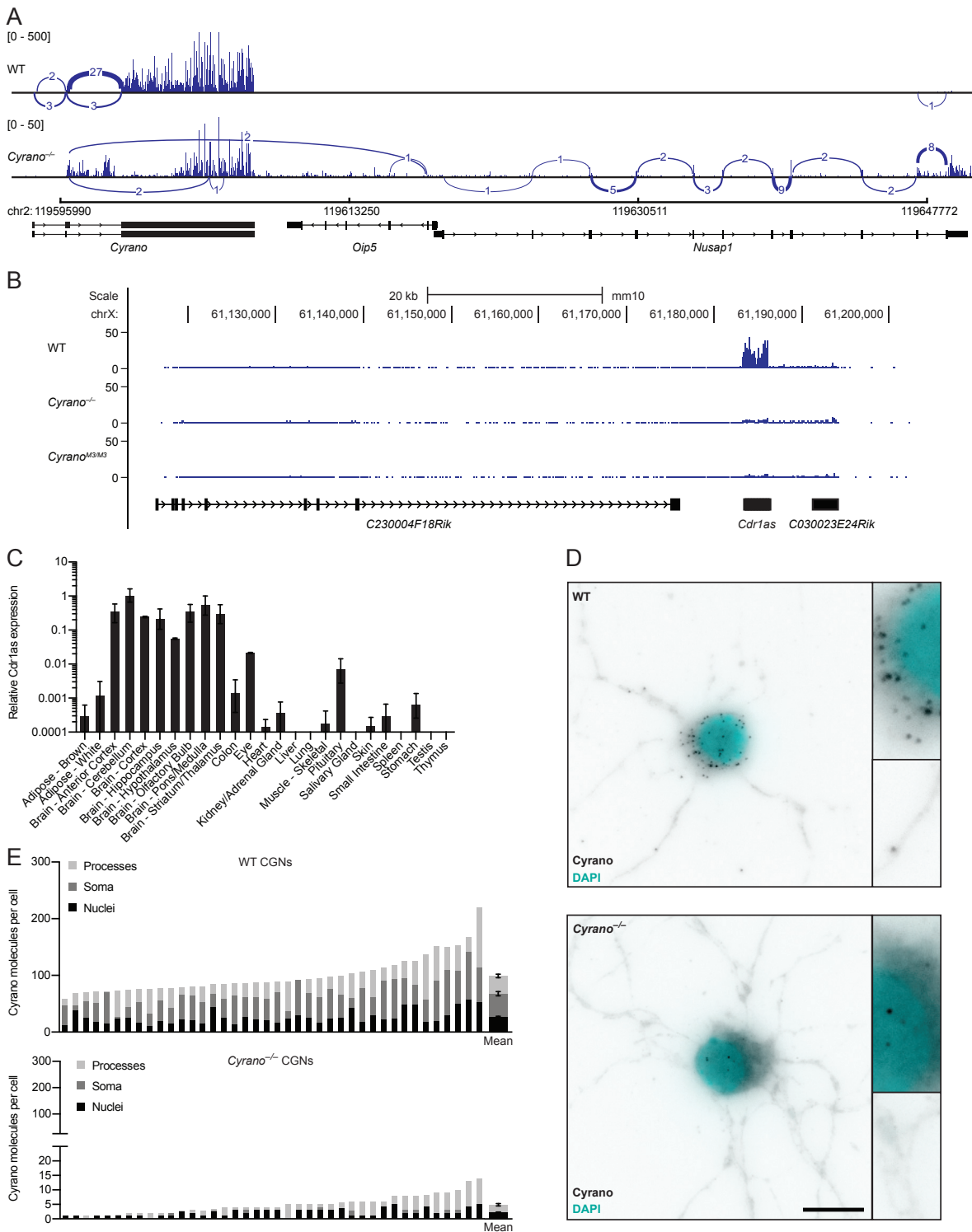


Figure S5. Cyrano Enables *Cdr1as* to Accumulate in Brain, Related to Figure 5

(A) Sashimi plot mapping splice junctions of Cyrano and *Nusap1* transcripts in wild-type and *Cyrano*^{-/-} cerebellum. Read density is shown on the y axis with the range given by the numbers in brackets above each track. Each arc represents a splice junction, and the numbers associated with each arc are the number of reads mapping to that splice junction.

(legend continued on next page)

-
- (B) Organization and expression of the extended murine *Cdr1as* locus. Shown are gene models (black boxes, exons; >>, introns) for the circularized *Cdr1as* exon (*Cdr1as*) and adjacent RIKEN cDNA genes that might be misannotated fragments of the host gene for the *Cdr1as* circRNA (Barrett et al., 2017). Otherwise, this panel is as in Figure 1A.
- (C) Relative *Cdr1as* expression in 25 tissues of 2-month-old C57BL/6J mice. Shown are mean *Cdr1as* levels, as determined by RT-qPCR, normalized to the geometric mean of the values for four housekeeping genes and relative to cerebellum (error bars, s.d.; n = 3 for each tissue).
- (D) Representative images from single-molecule FISH experiments probing for Cyrano (black) in wild-type (upper) and *Cyrano*^{-/-} (lower) CGNs, with insets showing increased magnification of portions of soma and processes. In Cyrano-deficient CGNs, a few Cyrano transcripts were detected, as expected for a probe set that extended beyond the deleted portion of Cyrano, but compared to wild-type, the number of molecules detected was greatly reduced. Otherwise, this panel is as in Figure 5D–E.
- (E) Quantitation of single-molecule FISH results obtained when probing for Cyrano in DIV11 wild-type (upper) and *Cyrano*^{-/-} (lower) CGNs. Otherwise, this panel is as in Figure 5D–E.

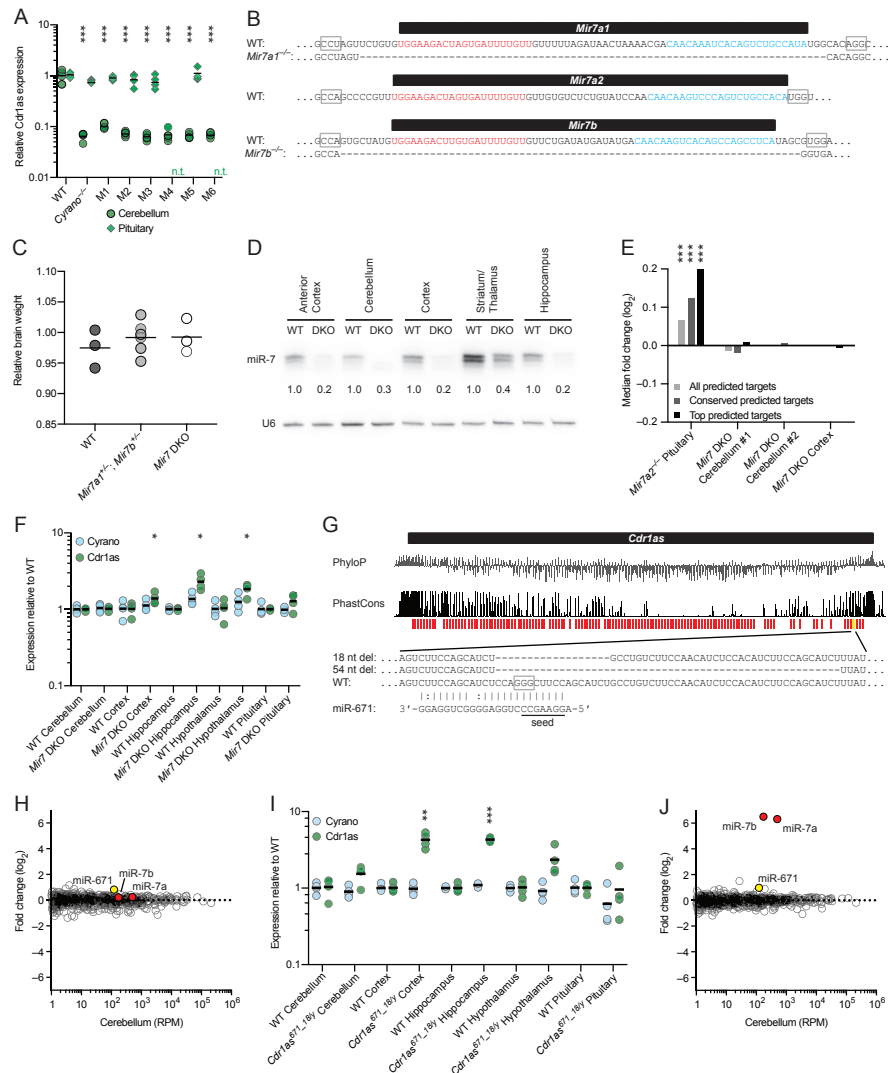


Figure S6. Cdr1as Is Regulated by miR-7 and miR-671, Related to Figure 6

(A) Importance of the miR-7 complementary site for the ability of Cyrano to influence Cdr1as levels in cerebellum. Cdr1as expression in wild-type and Cyrano mutant cerebellum (circle) was determined by RT-qPCR and plotted as in Figure 6D. For comparison, Cdr1as expression was also examined in pituitaries (diamond) of wild-type and some mutant mice (n.t., not tested). Statistical significance of the differences in Cdr1as level in each Cyrano mutant tissue compared to that in wild-type tissue is indicated (**p < 0.001, ANOVA with Dunnett's test). Otherwise, this panel is as in Figure 6D.

(B) Schematic of the three murine *Mir7* loci (black bars, pre-miRNAs; mature miRNAs and miRNA passenger strands are colored red and blue, respectively). PAM motifs used for Cas9-mediated mutagenesis are outlined (open gray boxes), and nucleotides deleted in *Mir7a1* and *Mir7b* mutants are indicated by dashes.

(C) Relative brain weights in P0 wild-type, *Mir7a1*^{-/-}; *Mir7b*^{+/-}, and *Mir7* DKO mice from three litters produced by crosses of double heterozygotes. Weights were mean-normalized for each litter. A significant difference in brain size between wild-type and DKO mice was not detected.

(D) miR-7 expression in wild-type and *Mir7* DKO brain. Shown is a northern blot measuring miR-7 levels in the indicated brain regions of 2-month-old wild-type and *Mir7* DKO female mice. Levels of miR-7 (upper panel) were normalized to those of U6 (lower panel) and reported relative to the wild-type level in each region. The residual miR-7 observed in DKO brain was presumably derived from the intact *Mir7a2* locus.

(E) Influence of miR-7 on predicted targets of miR-7 in cerebellum and cortex. #1 and #2 refer to two independent experiments (n = 3–4 per genotype for each experiment). For *Mir7* DKO tissues, the number of genes analyzed in each set ranged from 3809–3959 (all), 443–448 (conserved), 80–82 (top), and 2246–2376 (no site). Otherwise, this panel is as in Figure 4C.

(F) Influence of miR-7 on Cdr1as accumulation in brain and pituitary. Cdr1as levels were determined by RT-qPCR and plotted as in Figure 5B (green circles; black bars, mean; n = 4 per genotype). For comparison, Cyrano levels, determined in parallel, are also plotted (blue). Statistically significant changes in Cdr1as levels in *Mir7* DKO tissues compared to wild-type tissues are indicated (*p < 0.05; **p < 0.01; ***p < 0.001, unpaired two-tailed t test).

(G) Schematic of the murine Cdr1as locus. Shown below the gene model (black box, circularized exon), are conservation plots, as in Figure 1A, and lines indicating the location of either miR-7 sites (red) or the miR-671 site (yellow). Pairing of miR-671 to its slicing-competent site is diagramed below the conservation plots. The PAM motif used for Cas9-mediated mutagenesis is outlined (open gray box), and nucleotides deleted in the two different Cdr1as mutants are indicated by dashes.

(legend continued on next page)

-
- (H) miRNA profiling in wild-type and *Cdr1as*^{671_18/y} cerebellum. Shown are log₂-fold changes in mean miRNA levels observed between wild-type and *Cdr1as*^{671_18/y} cerebellum, as determined by small-RNA sequencing and plotted as a function of expression in wild-type cerebellum (n = 3 per genotype). Each circle represents one miRNA, showing results for all miRNAs expressed above 1 RPM (read per million miRNA reads) in wild-type cerebellum. Circles representing miR-7 paralogs and miR-671 are colored red and yellow, respectively. miR-671 increased 1.8-fold (adjusted p = 5.09 × 10⁻⁷, as determined by DESeq2), supporting the idea that the miR-671 complementary site in *Cdr1as* directs some degradation of miR-671 (Piwecka et al., 2017).
- (I) Influence of the miR-671 site on *Cdr1as* accumulation in brain and pituitary. Otherwise, this panel is as in (F).
- (J) miRNA profiling in wild-type and *Cyrano*^{-/-}; *Cdr1as*^{671_18/y} cerebellum. Otherwise, this panel is as in (H).